effects, or impairment of the quality of life (QOL) of the recipient. Fundamentally innovative antiarrhythmic strategies are, therefore, a matter of great concern to cardiologists.

In the heart, gap junctions (GJs) provide the pathways of intercellular current flow, enabling coordinated action potential propagation and contraction. GJ-channels are constructed from connexins (Cx), a multigene family of conserved proteins. In the mammalian heart, connexin43 (Cx43) is the most abundant and ubiquitous. Deranged expression and organization of Cx43 GJs in the ventricular muscles have been demonstrated in a variety of diseased hearts including ischemia, hypertrophy and inflammatory cardiomyopathy [1]. Such GJs remodeling is supposed to create arrhythmogenic substrates by modulating the propagation of excitation. X-ray irradiation has been shown to increase intercellular communication in the mouse skin [2] and rat alveolar epithelial cells in the lung [3] through an increase of expression of Cx43. If analogous up-regulation of Cx43 by radiation is induced efficiently in the diseased heart, it would provide a new perspective in the treatment of arrhythmias.

Radiotherapy using heavy-ions to treat deep-seated cancer was started at the National Institute of Radiological Sciences (NIRS) in Chiba, Japan in 1994 [4]. Charged-ion beams such as accelerated carbon-ions show a unique depth-dose distribution referred to as the Bragg peak in the target matter [5]. Those energetic ion beams decrease in kinetic energy thus reducing the velocity, finally stopping at a defined depth in the target object with high linear energy transfer (LET) [6], indicating a high relative biological effectiveness to X-rays (RBE). This gives advantages to heavy-ions over other radionucleid species in cancer therapy [5,6]. Based on this oncological experience, we hypothesized that such targeted heavy-ion beam irradiation (THIR) could also offer an advantage in causing up-regulation of Cx43 in the ischemic myocardium with minimal damage to the surrounding tissues.

2. Methods

Animal-handling followed the *Guide for the Care and Use of Laboratory Animals* (NIH Publication 85–23, revised 1996) with procedures approved by the Animal-Experimentation Ethics Committee of the Tokai University.

2.1. Animal model and heavy ion radiation

New Zealand white rabbits (n=48) weighing 3.5–4.0 kg were used. Non-transmural patchy myocardial infarction (MI) was created in 24 rabbits by microsphere injection (15 μm in diameter, 5×10^5/mL, 3 mL) into the coronary arteries by the transcatheter approach introduced from the carotid arteries [7]. The remaining 24 rabbits served as controls. Two weeks later, each 12 of MI and control rabbits received targeted THIR. Therefore, 4 animal groups were prepared: Control (C), C+THIR, MI, and MI+THIR.

We used carbon-ion beams provided by the Heavy Ion Medical Accelerator in Chiba (HIMAC) at NIRS, Japan [4]. The antero-lateral left ventricular (LV) free wall was focused for irradiation with carbon-ion beams (15 Gy) through the left anterior breast. The dose setting was confirmed appropriate in a pilot study. More details regarding the THIR procedures are described in the online data supplement.

2.2. Histology and immunohistochemistry

Ventricular tissue sections (12 μm thick slices) were fixed and embedded in paraffin. To recognize the MI and fibrosis region, the sections were stained by both hematoxylin/eosin (HE) and azan. The amounts of fibrosis were estimated from the binary images of azan-staining (Fig. 1). For immunostaining, the sections were incubated with an anti-Cx43 mouse monoclonal antibody (Chemicon), and then were treated with the secondary antibody (Alexa Flour 488 conjugated anti-mouse IgG). Some sections were also labeled with Alexa Flour 594 conjugated anti-cadherin, mouse monoclonal antibody (abcam). The immunolabelled sections were examined with a laser confocal microscope (LSM510, Version 2.02), and analyzed with the CLSM macro program (Carl Zeiss).

2.3. Real-time PCR and Western blotting

To quantify mRNA expression of Cx43 in the LV free wall, we performed a real-time PCR assay (Perkin-Elmer ABI Prism7700) [8]. GAPDH mRNA was used as an internal control. Sequence of PCR primers and sequence-specific probes are shown in the online data supplement.

The amount of Cx43 protein was evaluated by Western blotting [9]. The intensity of the Cx43 bands was quantified by densitometry and normalized to α-tubulin as the control.

2.4. In-vivo experiments

In-vivo electrophysiology experiments were conducted following open thorax surgery under anesthesia (α-chloralose, 80 mg/kg and urethane, 1000 mg/kg) [10]. An array of 8×8 monopolar electrodes (64Map) to cover 7×7 mm square (interpolar distance, 1 mm) was put on the LV wall between the left anterior descending branch (LAD) and left circumflex branch (LCx) of coronary arteries (Fig. 5A) [10]. The 64Map signals recorded simultaneously were acquired and processed by a computer. Activation time (AT) was defined as the interval from the beginning of QRS to the initial sharp negative deflection (min dV/dt). Recovery time (RT) was defined as the interval from the beginning of QRS to max dV/dt of T wave. The time difference between AT and RT in each electrogram was measured for the activation-recovery interval (ARI) as an index of action potential duration [11]. The dispersion of ARI (ARID) in the mapped area was estimated by the standard deviation of ARI at 64 electrodes [12]. The earliest AT within the electrode array was set down as 0 ms. Total activation time (TAT) was assessed as the delay between activation of the first and activation of the last electrode [12].

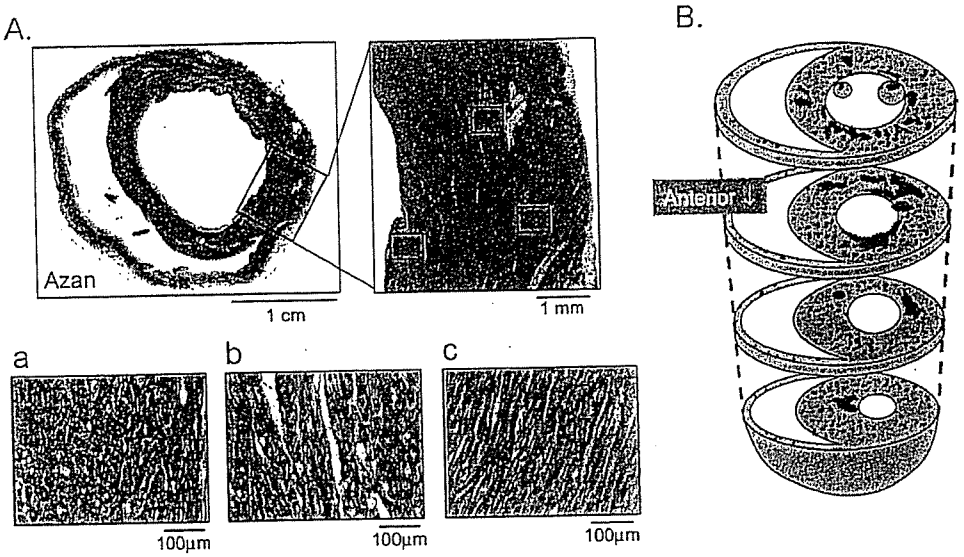

Fig. 1. Creation of non-transmural patchy myocardial infarction (MI) in rabbit hearts. A, a complete cross section of a low (left top), a moderate (right top) and a high magnification (bottom) of the ventricles 4 weeks after the creation of MI stained with HE/azan. Patchy fibrotic tissues (blue) are widely distributed in the subendocardial (a), mid-myocardial (b) and subepicardial (c) layers of the left ventricle (LV). B, 3-dimensional illustration of fibrotic tissue distribution (blue) in the same heart.

In order to assess the anisotropic conduction property, LV was paced at a cycle length of 200 ms (pulses of 1 ms duration and 1.2 times the threshold) via a pair of contiguous bipolar electrodes placed in the middle on the upper edge of the electrode array. Longitudinal (L) and transverse (T) directions of propagation were determined from the isochrone maps [9]. Conduction velocity (CV) was determined by linear regression of the isochrone distance vs. AT.

Propensity to VT/VF was tested by programmed electrical stimulation under norepinephrine infusion (0.1 μg/kg/min, i.v.). A pair of bipolar electrodes was placed on the epicardial surface near the LV apex. Following 5 basic stimuli (S1) at a cycle length of 200 ms, triple extra-stimuli (S2–S4) of double threshold were applied at progressively shorter coupling intervals.

2.5. Data analysis

Data are presented as means±SD. Data sets containing multiple groups were analyzed by 2-way layout analysis of variance and Bonferroni type multiple comparisons. Differences were considered statistically significant at a value of $P<0.05$.

3. Results

3.1. Standard light microscopy

Pathological features of rabbit hearts 4 weeks after creation of non-transmural MI by the microsphere injection method were analyzed in sections stained with HE and azan. Representative results (without radiation) are shown in Fig. 1. Multiple, small patchy infarctions with fibrosis surrounded by noninfarcted myocardium were recognized throughout the whole LV, and in part in the right ventricular (RV) free wall. Although the entire thickness of LV wall was involve, the fibrosis was more marked in the subendocardial region compared with subepicardial region. Qualitatively similar results were obtained from the hearts with and without THIR. The fibrosis areas estimated from the azan-staining of 4 whole cross sections in each heart from the base to the apex (Fig. 1) were 12.7±4.4% and 12.2±4.8% in MI and MI+THIR groups, respectively ($n=5$, $P>0.05$). Thus, THIR did not affect the amounts of fibrosis.

3.2. Immunostained Cx43 GJs in LV myocardium

Confocal microscopy for Cx43 immunolabeling was carried out in 6 hearts from all the 4 animal groups. Fig. 2A shows the representative effects of THIR in the control heart (without MI creation). Longitudinal sections of LV free wall myocardium were labeled for Cx43 (stained green) and cadherin (stained red). In Control, Cx43 formed clusters of punctate immunofluorescence domains confined to well-organized intercalated disks running across the longitudinal axis (panel a, arrows). Cadherin labeling showed a similar distribution to Cx43 (panel b). Double staining revealed the co-existence of Cx43 GJs and cadherin-containing fascia adherents confined to the intercalated disks, giving rise to their yellowish staining (panel c). In a rabbit 2 weeks after radiation (C+THIR), in contrast, Cx43 labeling was distributed not only at the intercalated disk but also at the lateral aspect of myocytes (panel d, arrowheads), whereas the normal distribution of cadherin was preserved (panel e).

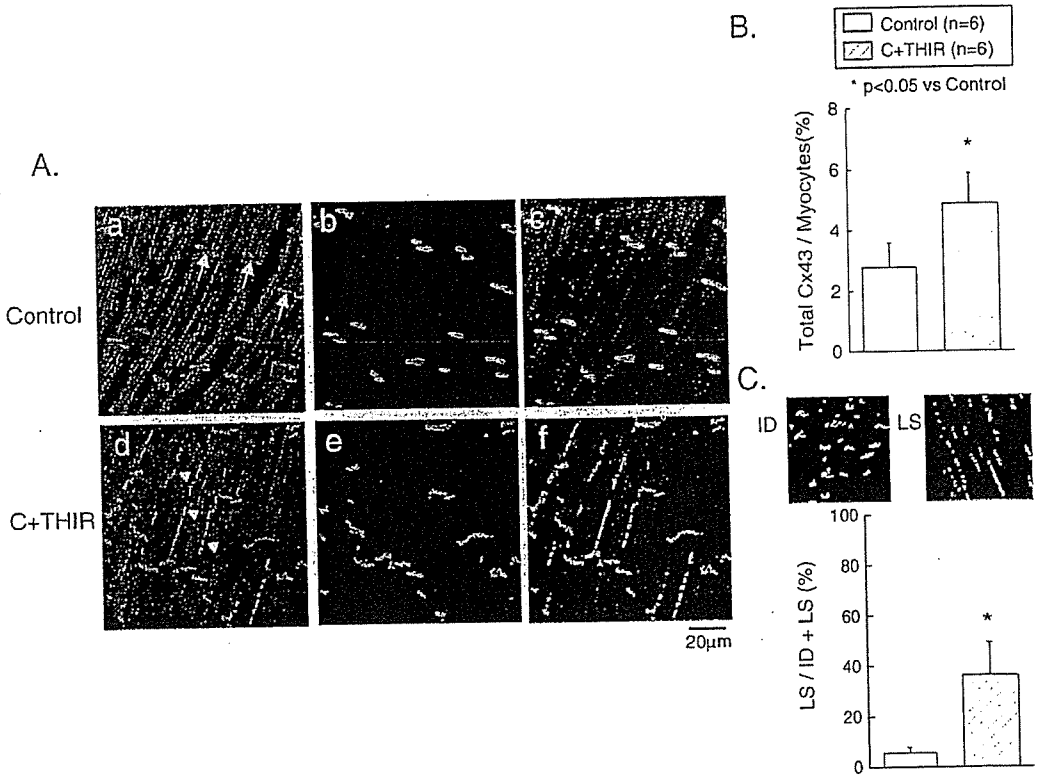

Fig. 2. Immunostained Cx43 gap junctions and fasciae adherentes in the LV myocardium of rabbits without MI. A, An LV myocardium sectioned longitudinally was labeled for Cx43 (green) and cadherin (red). Top, a section from a control heart; bottom, a section from a heart after targeted heavy ion irradiation (THIR). All images are single optical slices (confocal laser microscopy). Scale bar, 20 μm. B, The proportion of the total cell area occupied by Cx43 immunoreactive signal. Average values of 5 fields in each sample was obtained, and then means±SD of the values were calculated for each 6 samples. *$P<0.05$ vs. Control. C, Changes in the proportion of Cx43 labeled at the intercalated disk region (ID) and lateral cell surface (LS). (means±SD). Data were obtained from 12 rabbits (6 in each group). *$P<0.05$ vs. Control.

Double staining confirmed the dissociation of Cx43 from the intercalated disks (panel f). Similar derangements (lateralization) of Cx43 distribution were recognized in all C+THIR group. Fig. 2B shows the proportion of total cell area occupied by Cx43 immunoreactive signals. The radiation resulted in a significant increase in the Cx43 immunoreactive signals of 76%. Fig. 2C shows the proportion of Cx43 labeling at the lateral cell surface over the total labeling. The value in C+THIR was significantly higher (by 535%) than Control.

Fig. 3 show the effects of THIR on MI hearts. Representative changes of Cx43 immunolabeling patterns were compared in Fig. 3A at a low and a high magnification. In an MI heart (left), normal Cx43 labeling confined to the intercalated disks was preserved in the area distant from the infarcted tissue (patchy loss of myocytes indicated by arrowheads) (panels a, and c). In the area neighboring the infarcted tissue, Cx43 labeling was characterized either by prominent disorganization (panel e) or depletion (panel d). In an MI+THIR heart (right), immunoreactive Cx43 signals were increased throughout all of the LV tissues. This up-regulation was recognized not only in the normal zone distant from the patchy infarcted tissue (panel f), but also in the peri-infarct regions (panels g and h). The punctate Cx43 immunolabeling was distributed over the intercalated disk regions as well as lateral abutments of myocytes. Fig. 3B shows the proportion of total cell area occupied by the Cx43 immunoreactive signal obtained from the MI and MI+THIR groups. The irradiation resulted in a significant increase in Cx43 immunoreactive signals of 76%.

3.3. Expression of Cx43 mRNA and protein in the LV myocardium

The Cx43 mRNA level by a real-time PCR assay in the C+THIR specimens was significantly larger than that in Control specimens (by 18%) (Fig. 4A). The level in MIs, in contrast, decreased significantly compared with Controls (by 33%). Irradiation of MI rabbits (MI+THIR) reversed the down-regulation of Cx43 mRNA and increased by 88% compared with MI.

Cx43 protein amounts were estimated by Western blotting (Fig. 4B). The Cx43 antibodies recognized two bands migrating between 42 and 47 kDa. The Cx43 immunoblot signals were quantified by densitometry, and the intensity was normalized to that of α-tubulin on the same membrane. Irradiation of control rabbits (C+THIR) caused a significant increase in the total amount Cx43 protein by 88% compared with Control animals. In MI rabbits, the total Cx43 protein

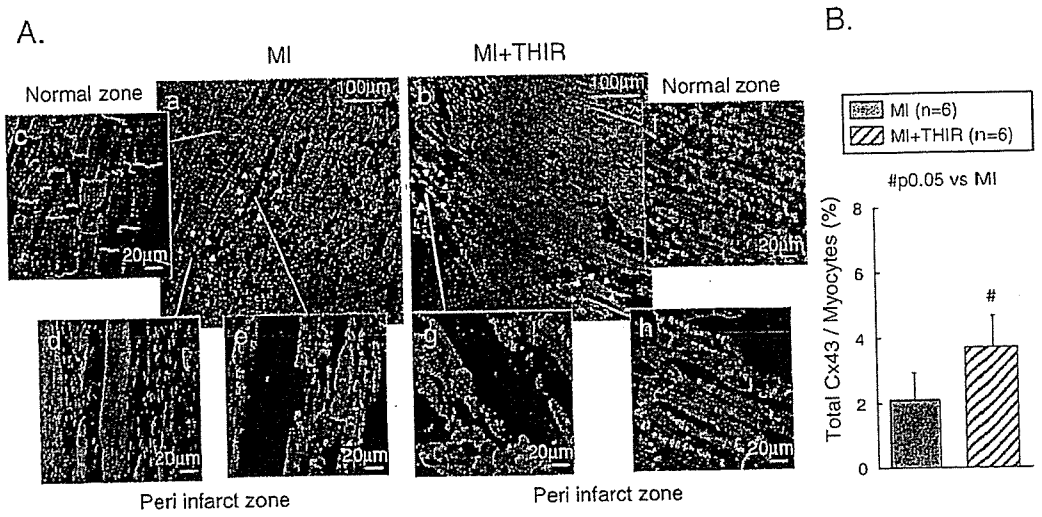

Fig. 3. Immunostained Cx43 gap junctions in the LV myocardium of rabbits with non-transmural MI. A, Left, a section from an MI heart; right, a section from a heart from MI+THIR. All images are single optical slices. Scale bar is 100 μm in panels (a) and (b), and 20 μm in panels (c) through (h). B, The proportion of total cell area occupied by Cx43 immunoreactive signal. Average values of 5 fields in each sample was obtained, and then means±SD of the values were calculated for each 6 samples. Data were obtained from 12 rabbits (6 in each group). #$P<0.05$ vs. MI.

levels significantly decreased compared with Controls (by 95%), and irradiation of MI rabbits (MI+THIR group) increased the level by 133% in comparison with unirradiated MI rabbits. We also estimated the density of the higher and lower molecular weight bands separately, which correspond to phosphorylated (P) and non-phosphorylated (NP) isoforms of Cx43, respectively. Irradiation caused appreciable increases in both Cx43-P and Cx43-NP in Control as well as in MI

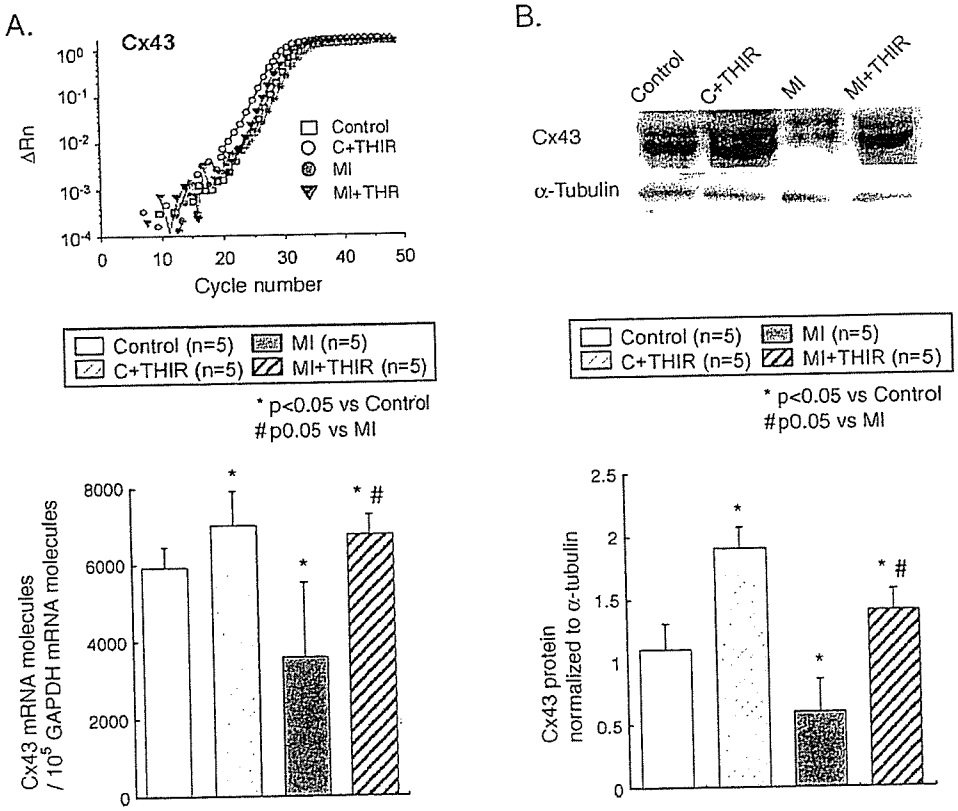

Fig. 4. Cx43 mRNA and protein levels. A, Cx43 mRNA levels were estimated by a real-time PCR and normalized to GAPDH. Top: Representative Cx43 PCR amplification plots for reactions. Change in fluorescence signal (ΔRn) is plotted against cycle number. Bottom: Cx43 mRNA levels normalized to GAPDH mRNA. Values are means±SD of each 5 rabbits in the 4 animal groups. B, Cx43 protein levels were estimated by Western blotting and normalized to α-tubulin. Values are means±SD of each 5 rabbits in the 4 animal groups. *$P<0.05$ vs. Control. #$P<0.05$ vs. MI.

rabbits. There were no significant differences among the four groups in the averaged ratio of P/NP (Control, 0.60; C+THIR, 0.84; MI, 1.00; MI+THIR, 0.96). Taken together, heavy-ion irradiation caused significant up-regulation of both mRNA and total protein levels of Cx43 in control as well as in MI hearts.

3.4. In-vivo electrophysiology

Fig. 5B illustrates representative AT and ARI maps on the LV anterior surface during the sinus rhythm (heart rate 197–238 bpm). In a Control rabbit, the activation proceeded quickly from paraseptal to lateral direction; TAT in the mapped area was 12 ms. ARIs were almost uniform, giving rise to a small ARID of 17 ms. In a C+THIR rabbit, the activation proceeded similarly (TAT 10 ms), but ARIs were homogeneously prolonged with ARID of 18 ms. In an MI rabbit, the activation proceeded much more slowly (TAT 32 ms). The ARI map showed tremendous regional variation, and ARID was increased up to 32 ms. In an MI+THIR rabbit, the AT map showed faster propagation (TAT 14 ms), and ARIs were more homogeneous than MI, causing less ARID (21 ms).

Data obtained from the 4 groups are summarized in Table 1. TAT was unchanged in C+THIR, but increased significantly in MI (by 89% from Control). The TAT in MI+THIR was significantly less than MI (by 42%), suggesting a reversal of the conduction delay. Both RI and ARI were significantly increased in C+THIR (by 10% and 11%, respectively). MI caused an appreciable prolongation of RT without affecting ARI compared with Control. In MI rabbits, RT and ARI were increased moderately after irradiation (MI+THIR), but the differences did not reach a statistical significance. In control rabbits, ARID was unaffected by irradiation. MI caused a significant increase in ARID (by 81%), and irradiation reversed the change.

Anisotropic conduction properties in the epicardial surface were examined in the 4 animal groups under constant pacing (cycle length of 200 ms) (Fig. 5C, D). In Control, the activation front proceeded at the highest speed in a direction parallel (longitudinal, L) to the subepicardial fiber orientation and at the slowest speed in a direction perpendicular to that (transverse, T). The isochrones showed an elliptical activation pattern. In the heart from a C+THIR rabbit, the elliptical

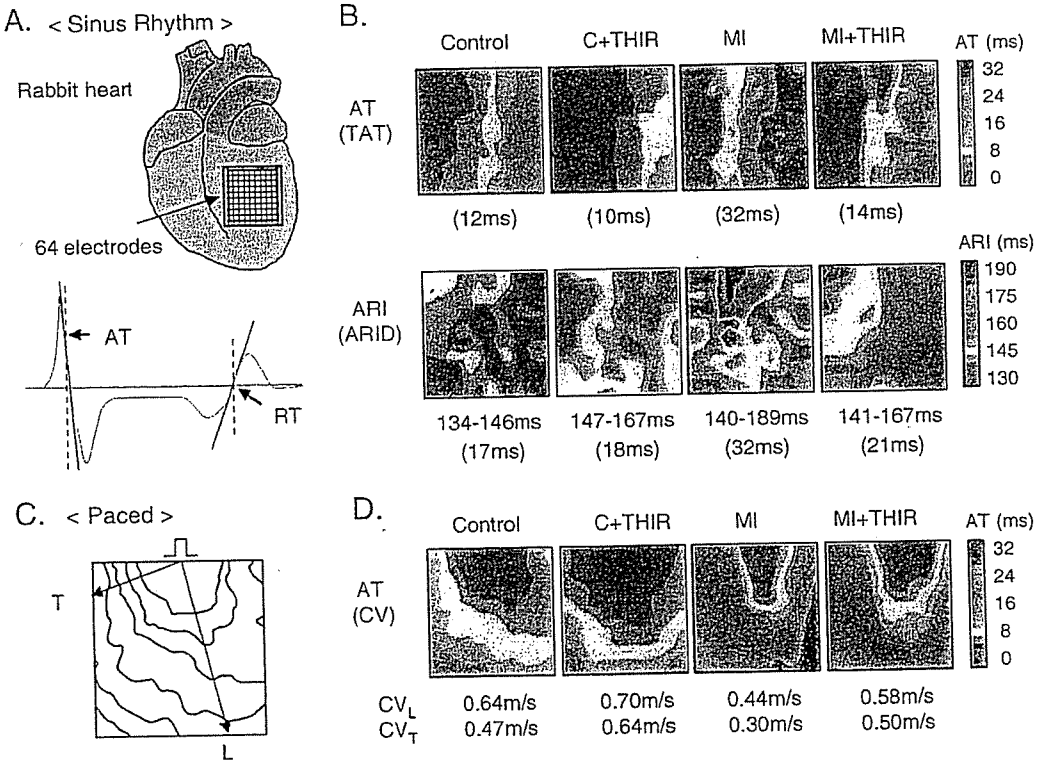

Fig. 5. Epicardial LV potential mapping. A, Sixty four monopolar electrodes were arranged as an 8×8 array to acquire the signals. Activation time (AT) at the recording site was identified by the initial sharp negative deflection (min dV/dt) of QRS. Recovery time (RT) was identified by the maximum upstroke slope (max dV/dt) of T wave. The time difference between AT and RT in each electrogram was measured for activation-recovery interval (ARI). B, Representative maps of AT and ARI during sinus rhythm. Total activation time (TAT) was measured from the maximal difference of AT. The dispersion of ARI (ARID) was estimated by the standard deviation of ARI at 64 electrodes. C, Anisotropic conduction properties were examined under constant pacing from the top middle of the electrode array. A line for longitudinal (L) propagation was drawn from the pacing site to the outer edge of the map, so as to cross the most widely spaced isochrones. A second line for transverse (T) propagation was drawn perpendicular to the first one. D, Representative maps of AT during the constant pacing. Conduction velocity in L and T direction (CV_L, CV_T) were measured from the isochrone maps.

Table 1
In-vivo electrophysiology

	Control (n=5)	C+THIR (n=5)	MI (n=5)	MI+THIR (n=5)
<Sinus rhythm>				
TAT (ms)	8.7±1.8	8.1±1.3	16.4±7.7*	9.5±2.7#
ARI (ms)	142±10	157±5*	146±18	160±8*
RT (ms)	150±10	165±6*	162±21*	169±8*
ARID (ms)	16.6±4.4	19.3±4.6	30.0±14.5*	18.8±4.5#
<Paced>				
CV_L (m/s)	0.66±0.14	0.72±0.18	0.48±0.10*	0.61±0.06#
CV_T (m/s)	0.45±0.04	0.67±0.20*	0.34±0.10*	0.51±0.09#
L/T	1.47±0.19	1.12±0.35*	1.54±0.61	1.22±0.19

Electrophysiological recordings were made in control rabbits without irradiation (Control, n=5), control rabbits after irradiation (C+THIR, n=5), myocardial infarction (MI) rabbits without irradiation (MI, n=5), and MI rabbits after irradiation (MI+THIR, n=5). Data were obtained either during sinus rhythm or under constant pacing at a cycle length of 200 ms. Values are means±SD. TAT, total activation time; RT, recovery time; ARI, activation-recovery interval; ARID, dispersion of ARI; CV_L, conduction velocity in longitudinal direction; CV_T, conduction velocity in transverse direction; L/T, anisotropic ratio of the conduction velocity. *P<0.05 vs. Control, #P<0.05 vs. MI.

pattern was less marked (more circular) because of acceleration of T propagation. In the heart from an MI rabbit, both L and T propagations were slowed down compared to Control, and the elliptical shape was slightly enhanced. In an MI+THIR rabbit, the activation pattern was more circular compared with MI alone, because of an acceleration of T propagation, which was more remarkable than the acceleration of L propagation. CVs in L and T directions (CV_L, CV_T) are summarized in Table 1. In control rabbits, irradiation caused a significant increase only in CV_T (by 49%), resulting in a significant decrease of the anisotropic ratio (L/T). In MI rabbits, both CV_L and CV_T were decreased compared with Control. Irradiation to MI rabbits (MI+THIR) caused significant increases of both CV_L and CV_T, but the change in CV_T (by 50%) was larger than that in CV_L (by 27%), resulting in a moderate reduction of L/T.

VT/VF induction was attempted by programmed stimulation in each 5 rabbits from the 4 animal groups. Representative ECG records in a Control, an MI and an MI+THIR rabbit are shown in Fig. 6A. Fig. 6B shows AT maps of 2 sequential beats during the VT/VF documented from the MI and MI+THIR rabbits. Fig. 6C summarizes the VT/VF incidence. In Control and C+THIR, no VT/VF was induced. In MI, 2 VF and 2 VT (one sustained >30 s, the other non-sustained) were induced. In MI+THIR, only one non-sustained VT (NSVT) was induced. Activation patterns during the NSVT were much more homogeneous than that during VF documented in MI rabbits (Fig. 6B).

3.5. Safety of irradiation

In both control and MI rabbits, THIR did not affect the hemodynamic parameters in echocardiography 2 weeks after the irradiation. The LV function in MI hearts was inhibited

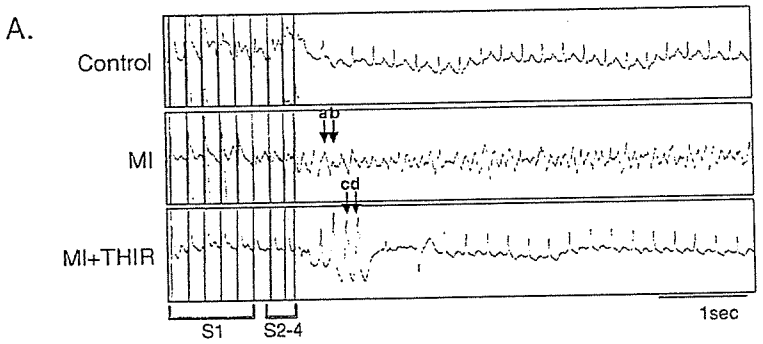

B. *AT map of two sequential beats during VT/ VF*

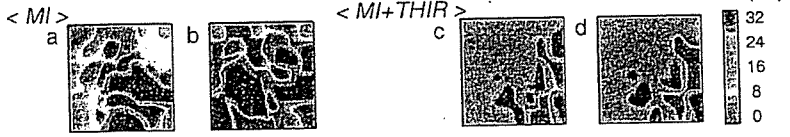

C. *Incidence of VT/ VF elicited by programmed stimulation*

	NSVT	SVT	VF	Vulnerability
Control (n=5)	0	0	0	0/5
C+THIR (n =5)	0	0	0	0/5
MI (n= 5)	1	1	2	4/5
MI+THIR (n=5)	1	0	0	1/5

Fig. 6. Induction of VT/VF by programmed stimulation under norepinephrine infusion (0.1 μg/kg/min, i.v.). A, Representative ECG recordings in Control, MI and MI+THIR rabbits. Following 5 basic stimuli (S1) at a cycle length of 200 ms, triple extra stimuli (S2–S4) were applied at progressively shorter coupling intervals. B, AT maps of two sequential beats during the VF and VT episodes in the MI and MI+THIR rabbits as presented in A. C, Incidence of VT/VF elicited by the programmed stimulation. SVT: sustained VT (>30 s), NSVT: non-sustained VT (<30 s). VFs were all sustained.

significantly compared with Control, and the irradiation did not ameliorate the hemodynamic parameters (online data supplement). Blood cell counts and chemistry were unaffected by the irradiation. However a circumscribed loss of hair began to appear on the left anterior chest soon after irradiation and remained for a year.

4. Discussion

4.1. The novel findings

Immunoreactive Cx43 fluorescent signals of MI hearts were reduced and disorganized notably. In addition, the Cx43 mRNA level and the amount of Cx43 protein in LV tissue, which were estimated by a real-time PCR and Western blotting, respectively, were markedly reduced in MI hearts. Most of these changes were reversed 2 weeks after THIR. *In-vivo* 64Map revealed that a reduction of CV in MI hearts was reversed by THIR. An increase of ARID in MI hearts was reversed by THIR. An increase of vulnerability for VT/VF induction by programmed stimulation in MI hearts was also reversed by THIR. All of these observations can be interpreted most likely by an improvement of electrical coupling of cardiac myocytes, causing a smoother propagation of excitation and homogeneous repolarization in the ventricle after MI.

Achieving up-regulation of Cx43 in the myocardium might be a target for novel antiarrhythmic therapies. The use of radiation to up-regulate the decreased Cx43 in diseased hearts has never been considered. Radiotherapy might be one of the only potential approaches for future therapeutic strategy through achieving an increase in the electrical coupling of cardiac cells via the up-regulation of GJs.

4.2. Functional consequences of Cx43 up-regulation and lateralization

In normal as well as in MI hearts, THIR caused up-regulation of Cx43 and an increase of Cx43 distribution at the lateral cell abutments (lateralization). These changes would have a variety of functional consequences. The activation maps under constant pacing showed that the irradiation increased CVs and the effect was greater in T than L propagation, giving rise to a reduction of the anisotropic ratio (L/T). This observation suggests that Cx43 up-regulated and distributed more laterally may form functional GJs even though Cx43 was dissociated from cadherin. In rat atria in which atrial fibrillation (AF) was induced by 24 h of rapid pacing, Polontchouk et al. [13] showed up-regulation and marked lateralization of immunoreactive Cx43, like in human AF patients. The Cx43 remodeling was associated with a greater increase of CV_T than CV_L, resulting in a reduction of the anisotropic ratio. In experiments using isolated normal ventricular myocardium, pharmacological uncoupling of GJs (by heptanol or palmitoleic acid) was shown to cause greater inhibition of T propagation than L propagation [14,15]. A higher susceptibility of T propagation than L propagation in response to GJ uncoupling was also demonstrated in a computer simulation [16]. Accordingly, the total up-regulation of Cx43 by THIR could also contribute to the preferential improvement of T propagation.

It appears that lateralization of gap junctions is a prominent feature of diseased hearts, including a variety of ischemic and hypertrophic cardiomyopathies [1,16]. Functional implication of this feature is variable. In experiments using aged rabbits, Dhein and Hammerrath [17] found reduced CV_T and enhanced anisotropy (CV_L was preserved). Those changes were associated with prominent increase of fibrosis separating myocardial cells and lateralization of Cx43. The extensive fibrosis might have offset the effects of GJ lateralization. Alternatively, the displaced Cx43 GJs could be degraded and non-functional [1]. Since we used young rabbits in the present study, the control hearts with and without THIR had no appreciable collagen strands separating myocardial fibers. In MI hearts, in contrast, there existed substantial amounts of fibrosis at the regions of patchy infarction. Despite of such fibrosis, THIR improved the T propagation.

As to the role enhanced GJ lateralization in arrhythmogenesis, there are 2 possibilities. If the GJs function normally, they would ameliorate the inhibition of T propagation resulting from functional and structural uncoupling of cardiac cells, and may reduce the risk for microscopic anisotropic reentry based on the extremely slow T propagation [18,19] and the lateral inhomogeneity of repolarization. The present results seem consistent with this prediction. If the lateral GJs are degraded and non-functional, the conductivity and electrical homogeneity of the heart will be hampered by the dislocation in favor of reentrant excitations. In a simulation study using a two-dimensional model of myocardial cell architecture, Spach and Heidlage [20] suggested the stochastic nature of normal propagation at a microscopic level based on the normal polar distribution of GJs provides a considerable protective effect against arrhythmias by reestablishing the general trend of wave-front movement after small variations in excitation events occur.

Cx43 is a phosphoprotein, and phophorylation/dephosphorylation of Cx43 plays important roles in the regulation of Cx43 protein turnover dynamics (trafficking, plaque assembly, disassembly and degradation) as well as GJ channel gating properties [21]. We estimated the relative expression of P and NP isoforms of Cx43 from 2 bands recognized in Western blotting. The results may suggest that THIR increases both Cx43-P and Cx43-NP without affecting their P/NP ratio. However, more extensive Western blots using isoform-specific Cx43 antibodies will be required to resolve the issue.

4.3. Mechanisms of Cx43 up-regulation by irradiation

In the field of oncology, it has been demonstrated in many *in-vitro* and *in-vivo* studies that intercellular communication

is enhanced by photon [2,3] or ionizing radiation [22,23] via up-regulation of Cx43 GJs at mRNA and protein levels. The increase of intercellular communication is believed to play an important role for the enhancement of radiation-induced effects such as modulation of gene expression, mutagenesis and cell survival (bystander effect) [24–26]. As to the molecular mechanisms responsible for the radiation-induced Cx43 up-regulation, the information available is still limited. Using deletion and site-directed mutagenesis analyses in human fibroblasts and HeLa cells, Glover et al. have demonstrated that 2 consensus sites, nuclear factor of activated T-cells (NFAT) and activator protein (AP1), are responsible for the major activation of the Cx43 promoter in response to low doses of ionizing radiation [23] A similar molecular mechanism could be involved in the THIR-induced up-regulation in mammalian cardiac cells, but the issue remains to be investigated.

4.4. What other methods could be considered to achieve similar results?

Several procedures have been proposed by previous investigators to increase the electrical coupling of ventricular myocytes through an increase of Cx43 protein. Those include endothelin-1, angiotensin-II, thyroid hormones, AAP10 and nitrofen [27–30]. As to the therapeutic challenge to ameliorate arrhythmogenic substrates, however, all of these procedures have significant limitations in their clinical feasibility because of their low efficiency, undesirable cardiovascular and other side effects. We believe that THIR might be the first clinically feasible procedure, although further experimental studies using large animals will be required to substantiate this proposal.

4.5. Limitations

1) Because the rabbit heart is smaller and the heart rate is faster than human, higher irradiation accuracy was demanded in the present study. It was practically difficult to synchronize the heart motion completely to correspond to the radiation release. In addition to the targeted anterolateral LV free wall, other regions of LV might have been subjected to the irradiation. 2) The time dependent expression of Cx43 and the minimum irradiation energy for the appearance of the first antiarrhythmic effect were not examined.

5. Conclusion

Heavy-ion energy increases Cx43 expression of the ventricle in MI rabbits and consequently improves the conductivity, decreases the spatial heterogeneity of repolarization, and reduces the VT/VF vulnerability. Targeted heavy-ion irradiation to the heart could have the potential to become a new antiarrhythmic preventive therapy for MI patients through the restoration of cell-to-cell electrical coupling.

Acknowledgments

This work was supported by Grants-in-Aid for Scientific Research (B) 17390236 from JSPS and Tokai University School of Medicine Research Aid. We are grateful to many colleagues for their technical support: Atsushi Matsuzaki, Kazutane Usui, Yoshiaki Deguchi, Yuji Ikari, Nobue Kumaki, Sachie Tanaka, Noboru Kawabe, Hideaki Hasegawa, Yoshiro Shinozaki, Jobu Itoho in Tokai University; Jong-Kook Lee, Yoshiko Takagishi, Akiko Matsumiya, Kyoko Harada, Mayumi Hojo in Nagoya University; Takeshi Murakami, Kumie Nojima in the HIMAC Cooperative Research Project; Norio Sugimoto in the SANWAKAGAKU laboratory; Norihiko Mishima, Masaya Sakai, Satoshi Yamazaki in FUKUDA DENSHI,. Co Ltd; Daisuke Araki, Takashi Akamatsu, Michinari Kaneko in UNIQUE MEDICAL,. Co Ltd; and Daisuke Nakata in Ela Medical,. Co Ltd.

Appendix A. Supplementary data

Supplementary data associated with this article can be found, in the online version, at doi:10.1016/j.cardiores.2006.09.010.

References

[1] Severs NJ, Coppen SR, Dupont E, Yeh HI, Ko YS, Matsushita T. Gap junction alterations in human cardiac disease. Cardiovasc Res 2004;62:368–77.
[2] Liu K, Kasper M, Bierhause A, Langer S, Muller M, Trott KR. Connexin 43 expression in normal and irradiated mouse skin. Radiat Res 1997;147:437–41.
[3] Kasper M, Traub O, Reimann T, Bjermer L, Grossmann H, Muller M, et al. Upregulation of gap junction protein connexin 43 in alveolar epithelial cells of rats with radiation-induced pulmonary fibrosis. Histochem Cell Biol 1996;106:419–24.
[4] Kanai T, Endo M, Minohara S, Miyahara N, Koyama I, Tomura H, et al. Biophysical characteristics of HIMAC clinical irradiation system for heavy-ion radiation therapy. Int J Radiat Oncol Biol Phys 1999;44:201–10.
[5] Debus J, Jackel O, Kraft G, Wannenmacher M. Is there a role for heavy ion beam therapy? Recent Results Cancer Res 1998;150:170–82.
[6] Koike S, Ando K, Oohira C, Fukawa T, Lee R, Takai N, et al. Relative biological effectiveness of 290 MeV/u carbon ions for the growth delay of a radioresistant murine fibrosarcoma. J Radiat Res 2002;43:247–55.
[7] Tanaka E, Hattan N, Ando K, Ueno H, Sugio Y, Mohammed MU, et al. Amelioration of microvascular myocardial ischemia by gene transfer of vascular endothelial growth factor in rabbits. J Thorac Cardiovasc Surg 2000;120:720–8.
[8] Niwa N, Yasui K, Opthof T, Takemura H, Shimuzu A, Horiba M, et al. $Ca_v3.2$ subunit underlies the functional T-tye Ca^{2+} channel in murine hearts during the embryonic period. Am J Physiol 2004;286:H2257–63.
[9] Uzzaman M, Honjo H, Takagishi Y, Emdad L, Magee AI, Severs NJ, et al. Remodeling of gap junctional coupling in hypertrophied right ventricles of rats with monocrotaline-induced pulmonary hypertension. Circ Res 2000;86:871–8.
[10] Yoshioka K, Amino M, Usui K, Sugimoto A, Matsuzaki A, Kohzuma K, et al. Nifekalant hydrochloride administration during cardiopulmonary resuscitation improves the transmural dispersion of myocardial repolarization. Circulation J 2006;70:1200–7.
[11] Yoshioka K, Gao DW, Chin M, Stillson C, Penades E, Lesh M, et al. Heterogeneous sympathetic innervation influences local myocardial repolarization in normally perfused rabbit hearts. Circulation 2000;101:1060–6.

[12] Dhein S, Muller A, Gerwin R, Klaus W. Comparative study on the proarrhythmic effects of some antiarrhythmic agents. Circulation 1993;87:617–30.
[13] Polontchouk L, Haefliger J-A, Ebelt B, Schaefer T, Stuhlmann D, Mehlhorn U, et al. Effects of chronic atrial fibrillation on gap junction distribution in human and rat atria. J Am Coll Cardiol 2001;38:883–91.
[14] Delmar M, Michaels DC, Johnson T, Jalife J. Effects of increasing intercellular resistance on transverse and longitudinal propagation in sheep epicardial muscle. Circ Res 1987;60:780–5.
[15] Dhein S, Krusemann K, Schaefer T. Effects of the gap junction uncoupler palmitoleic acid on the activation and repolarization wavefronts in isolated rabbit hearts. Br J Pharmacol 1999;128:1375–84.
[16] Jongsma HJ, Wilders R. Gap junctions in cardiovascular disease. Circ Res 2000;86:1193–7.
[17] Dhein S, Hammerath S-B. Aspects of the intercellular communication in aged hearts: effects of the gap junction uncoupler palmitoleic acid. Naunyn-Schmiedeberg's Arch Pharmacol 2001;364:397–408.
[18] Spach MS, Josephson ME. Initiating reentry: the role of nonuniform anisotropy in small circuits. J Cardiovasc Electrophysiol 1994;5:182–209.
[19] Koura T, Hara M, Takeuchi S, Ota K, Okada Y, Miyoshi S, et al. Anisotropic conduction properties in canine atria analyzed by high-resolution optical mapping. Preferential direction of conduction block changes from longitudinal to transverse with increasing age. Circulation 2002;105:2092–8.
[20] Spach MS, Heidlage JF. The stochastic nature of cardiac propagation at a microscopic level. Electrical description of myocardial architecture and its application to conduction. Circ Res 1995;76:366–80.
[21] Lampe PD, Lau AF. The effects of connexin phosphorylation on gap junctional communication. Int J Biochem Cell Biol 2004;36:1171–86.
[22] Azzam EI, de Toledo SM, Gooding T, Little JB. Intercellular communication is involved in the bystander regulation of gene expression in human cells exposed to very low fluences of alpha particles. Radiat Res 1998;150:497–504.
[23] Glover D, Little JB, Lavin MF, Gueven N. Low dose ionizing radiation-induced activation of connexin43 expression. Int J Radiat Biol 2003;79:955–64.
[24] Azzam EI, de Toledo SM, Little JB. Expression of connexin 43 is highly sensitive to ionizing radiation and other environmental stresses. Cancer Res 2003;63:7128–35.
[25] Little JB, Azzam EI, de Toledo SM, Nagasawa H. Bystander effects: intercellular transmission of radiation damage signals. Radiat Prot Dosim 2002;99:159–62.
[26] Azzam EI, de Toledo SM, Little JB. Direct evidence for the participation of gap junction-mediated intercellular communication in the transmission of damage signals from alpha-particle irradiated to nonirradiated cells. PNAS 2001;98:473–8.
[27] Polontchouk L, Ebelt B, Jackels M, Dhein S. Chronic effects of endothelin 1 and angiotensin II on gap junctions and intercellular communication in cardiac cells. FASEB J 2002;16:87–9.
[28] Tribulova N, Shneyvays V, Mamedova LK, Moshel S, Zinman T, Shainberg A, et al. Enhanced connexin-43 and alpha-sarcomeric actin expression in cultured heart myocytes exposed to triiodo-L-thyronine. J Mol Histol 2004;35:463–70.
[29] Muller A, Schaefer T, Linke W, Tudyka T, Gottwald M, Klaus W, et al. Actions of the antiarrhythmic peptide AAP10 on intercellular coupling. Naunyn-Schmiedeberg's Arch Pharmacol 1997;356:76–82.
[30] Gonzalez-Reyes S, Fernandez-Dumont V, Calonge WM, Martinez L, Tovar JA. Expression of Connexin 43 in the hearts of rat embryos exposed to nitrofen and effects of vitamin A on it. Pediatr Surg Int 2006;22:61–5.

The EMBO Journal (2006) 25, 2315–2325 | © 2006 European Molecular Biology Organization | All Rights Reserved 0261-4189/06
www.embojournal.org

THE EMBO JOURNAL

Crystal structure of CHP2 complexed with NHE1-cytosolic region and an implication for pH regulation

Youssef Ben Ammar[1,4], Soichi Takeda[2,3,4], Takashi Hisamitsu[1], Hidezo Mori[2] and Shigeo Wakabayashi[1,*]

[1]Department of Molecular Physiology, National Cardiovascular Center Research Institute, Suita, Osaka, Japan, [2]Department of Cardiac Physiology, National Cardiovascular Center Research Institute, Suita, Osaka, Japan and [3]Laboratory of Structural Biochemistry, RIKEN Harima Institute at SPring-8, Kouto, Mikazuki-cho, Sayo, Hyogo, Japan

The plasma membrane Na^+/H^+ exchangers (NHE) require calcineurin B homologous protein (CHP) as an obligatory binding partner for ion transport. Here, we report the first crystal structure of CHP (CHP2 isoform) in complex with its binding domain in NHE1. We show that the cytoplasmic α-helix of NHE1 is inserted into the hydrophobic cleft formed by N- and C-lobes of CHP2 and that the size and shape of this crevice together with hydrogen bond formation at multiple positions assure a high degree of specificity for interaction with NHE members. Structure-based mutagenesis revealed the importance of hydrophobic interactions between CHP/NHE1 for the function of NHE1. Furthermore, the crystal structure shows the existence of a protruding CHP-unique region, and deletion of this region in CHP2 inhibited the NHE1 activity by inducing the acidic shift of intracellular pH dependence, while preserving interaction with NHE1. These findings suggest that CHP serves as an obligatory subunit that is required both for supporting the basic activity and regulating the pH-sensing of NHE1 via interactions between distinct parts of these proteins.

The EMBO Journal (2006) 25, 2315–2325. doi:10.1038/sj.emboj.7601145; Published online 18 May 2006
Subject Categories: membranes & transport; structural biology
Keywords: calcineurin homologous protein; crystal structure; Na^+/H^+ exchanger; pH regulation

Introduction

Maintenance of intracellular pH (pH_i), Na^+ concentration, and cell volume is crucial for all living cells to survive and to ensure a variety of cellular functions, such as cell metabolic processes, muscle contraction, secretion, and higher-order brain activity. The Na^+/H^+ exchanger (NHE) is an important transporter regulating such ionic homeostasis and catalyzing the electroneutral countertransport of Na^+ and H^+ through the plasma membrane and other intracellular organellar membranes in various animal species (Wakabayashi *et al*, 1997; Counillon and Pouyssegur, 2000; Putney *et al*, 2002; Orlowski and Grinstein, 2004; Zachos *et al*, 2005). Of the nine different NHE isoforms identified to date (NHE1–NHE9), the ubiquitous isoform NHE1 has been studied most extensively. NHE1 is known to be activated rapidly in response to various extracellular stimuli, such as hormones, growth factors, and mechanical stressors (Wakabayashi *et al*, 1997; Orlowski and Grinstein, 2004). Such activation of NHE1 is often linked to various diseases. For example, elevated NHE1 activity is thought to be a risk factor causing heart failure and hypertrophy, as evidenced by the remarkable protective effects of specific inhibitors (Karmazyn, 2001; Engelhardt *et al*, 2002). Regulation of NHE1 is thought to occur through interaction of multiple signaling molecules with the carboxyl (C)-terminal cytoplasmic domain of NHE1 and subsequent conformational change of the amino (N)-terminal transmembrane domain responsible for catalyzing NHE (see Figure 1A for membrane topology). Importantly, this regulation of NHE1 is attributable to a change in the affinity for intracellular H^+. A previous biochemical experiment using membrane vesicles suggested that the exchangers possess a cytoplasmic 'H^+-modifier' or 'pH-sensor' site(s), distinct from the H^+-transport site (Aronson *et al*, 1982; Wakabayashi *et al*, 2003a). The exchangers were thus considered to be activated through conformational changes caused by protonation of this regulatory site. Our recent study, using cells expressing NHE isoforms (NHE1–3), further supported this concept by measuring the reverse reaction of exchange (Na^+ efflux) (Wakabayashi *et al*, 2003a). However, another recent study reported an allosteric model with no additional H^+-modifier site to explain the sigmoidal cytosolic H^+ dependence (Lacroix *et al*, 2004).

Of the signaling molecules that interact with the exchanger, calcineurin B (CNB) homologous protein (CHP) is particularly important. CHP was initially identified as a protein (p22) involved in vesicular transport (Barroso *et al*, 1996) and that interacts with NHE (Lin and Barber, 1996). CHP is a Ca^{2+}-binding protein with EF-hand motifs and is myristoylated at the N-terminus (Gly2) (Barroso *et al*, 1996; Lin and Barber, 1996). To date, three CHP isoforms with different tissue expression patterns have been identified in mammalian tissues. While CHP1 is expressed ubiquitously in virtually all tissues, the expression of CHP2 is restricted to cancer cells (Pang *et al*, 2002) and the small intestine (Inoue *et al*, 2003), and that of CHP3 (also called tescalcin) is restricted to the heart, brain, stomach, and testis (Mailander *et al*, 2001; Perera *et al*, 2001; Gutierrez-Ford *et al*, 2003). Previously, we reported that CHP (at least CHP1 and CHP2) is an essential cofactor supporting the physiological activity of the plasmalemmal NHE by interacting with the juxtamembrane cyto-

*Corresponding author. Department of Molecular Physiology, National Cardiovascular Center Research Institute, Fujishirodai 5-7-1, Suita, Osaka 565-8565, Japan. Tel.: +81 6 6833 5012; Fax: +81 6 6835 5314; E-mail: wak@ri.ncvc.go.jp
[4]These authors contributed equally to this work

Received: 5 December 2005; accepted: 24 April 2006; published online: 18 May 2006

Table I Data collection, phasing and refinement statistics

	High resolution data	MAD		
Data collection				
Space group	$P4_3$		$P4_3$	
Cell dimensions				
a, *b*, *c* (Å)	49.96, 49.96, 103.2		49.96, 49.96, 103.2	
α, β, γ (deg)	90, 90, 90		90, 90, 90	
		Peak	*Inflection*	*Remote*
Wavelength	1.0000	0.7270	0.7266	1.0000
Resolution (Å)	50–2.7	50–3.0 (3.11–3.00)	50–3.0 (3.11–3.00)	50–3.0 (3.11–3.00)
R_{merge}[a]	4.8 (25.1)	0.084 (0.311)	0.073 (0.297)	0.072 (0.330)
$I/\sigma I$[b]	17.3 (4.5)	14.9 (4.1)	15.9 (5.0)	15.8 (3.6)
Completeness (%)[b]	97.3 (83.1)	98.5 (87.5)	98.5(87.5)	97.8 (80.9)
Redundancy[b]	4.0 (3.1)	7.2 (5.6)	7.3 (5.7)	7.1 (5.3)
Refinement				
Resolution (Å)	50–2.7			
No. reflections	6746			
R_{work}/R_{free}	0.218/0.287			
No. atoms				
Protein	1674			
Ligand/ion	2			
B-factors				
Protein	72.5			
Ligand/ion	70.5			
R.m.s. deviations				
Bond lengths (Å)	0.005			
Bond angles (deg)	1.00			
Ramachandran plot (%)				
Favorable	87.2			
Allowed	12.8			
Generously allowed	0			
Disallowed	0			

[a]$R_{merge} = \sum_{hkl} \sum_i |I_i(hkl) - \langle I(hkl) \rangle| / \sum_{hkl} \sum_i I_i(hkl)$, where $I_i(hkl)$ is the *i*th intensity measurement of reflection *hkl*, and $\langle I(hkl) \rangle$ is its average.
[b]Highest resolution shell is shown in parentheses.

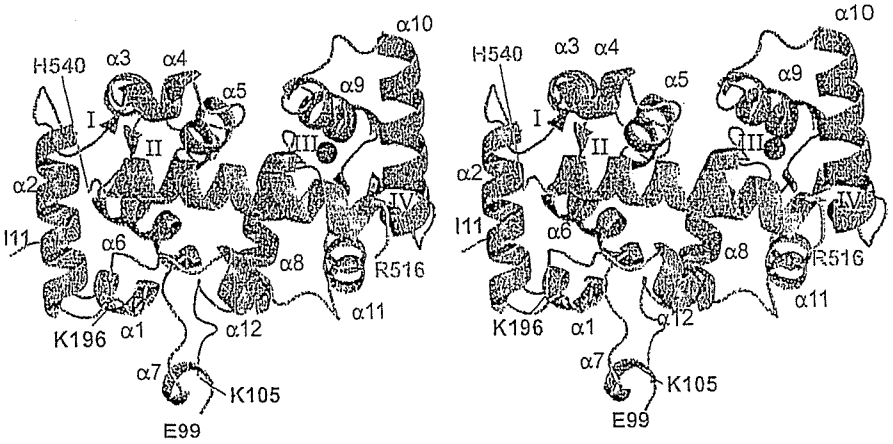

Figure 2 Stereo view of the CHP2/NHE1-peptide complex showing the overall structure. N- and C-lobes of CHP2 are colored *red* and *blue*, respectively. The NHE1 peptide is colored *green*. *Pink* spheres represent the two yttrium ions coordinated by EF3 and EF4.

the overall structure of the complex CHP2/NHE1-peptide. The structural model contains 181 amino acids from CHP2 (Ile11–Glu99 and Lys105–Lys196), and 25 amino acids from NHE1 fragment (Arg516–His540). The polypeptide chain of CHP2 with dimensions of 55 × 47 × 28 Å is folded into two globular domains (N- and C-terminal lobes) composed of 12 α-helices (α1–α12) and four short β-strands (β1–β4). Two Y^{3+} ions were found to associate with EF3 and EF4 in the C-lobe (Figure 2), consistent with biochemical data showing the high-affinity binding of Y^{3+} (~1 nM) to CHP2 (Supplementary Figure 1). The overall structure of CHP2 is close to the Ca^{2+}-bound form of NHE-free CHP1, which was solved recently (Naoe *et al*, 2005; Supplementary Figure 2). Indeed, the distances between metal ions and coordinating oxygen atoms are almost the same for Y^{3+} in CHP2 (2.38 ± 0.2 Å) and Ca^{2+} in CHP1 (2.40 ± 0.1 Å). In addition, the

Y^{3+}-bound form of CHP2 preserved the ability to interact with the full-length NHE1 (Supplementary Figure 1). Therefore, we consider our solved structure compatible with the Ca^{2+}-bound form of CHP2. The overall structure of CHP2 is also similar in folding topology to the structures of other EF-hand-containing proteins, including CNB (Kissinger *et al*, 1995), K^+-channel interacting protein (KChIP1) (Zhou *et al*, 2004; Supplementary Figure 2), AtCBL2 (Nagae *et al*, 2003), NCS-1 (Bourne *et al*, 2001), neurocalcin (Vijay-Kumar and Kumar, 1999), and CIB (Gentry *et al*, 2005). A common structural feature of these proteins is that they all have four EF-hands in pairs such that EF1 and EF2 form the N-lobe and EF3 and EF4 form the C-lobe. However, some local differences were observed between CHP2 and CNB or between CHP2 and KChIP1. For example, the orientation of EF-hand α-helices is different among these molecules because of the swiveling motion between the N- and C-lobes of each molecule, although each pair of EF hands is relatively fixed via hydrogen bonds. This may explain the incomplete superposition between overall structures of CHP2 and CNB (root mean square deviation, r.m.s.d. 1.7 Å), in contrast to the relatively good superposition between the N-lobes or between the C-lobes themselves (r.m.s.d. 1.3 or 1.0 Å, respectively). Although CHP2 and CNB have about 36% identity in their amino-acid sequences (Figure 1C), CHP2 coordinates two Ca^{2+} ions in EF3 and EF4, unlike CNB capable of coordinating four Ca^{2+} ions in its four EF-hands (Kissinger *et al*, 1995). Lack of Ca^{2+}-coordination in EF1 and EF2 would be derived from significant deviation from the canonical EF-hand sequence and resulting atypical structure, as described previously in detail (Naoe *et al*, 2005).

The most remarkable difference between CHP2 and other calcium binding proteins is that the N- and C-lobes of CHP2 are linked by a long flexible region, which protrudes by a length of about 14 Å for the determined region (Figure 3A). This domain, referred to as the CHP-unique region, was not found in other Ca^{2+}-binding proteins. Five residues, Thr100 to Lys104, were not assigned in the structure due to the absence of their electron density map. Particularly, the region from aa 93–108 did not make any contact with other regions of CHP2. In addition, we found that the side chain oxygen atoms of Asp95 in this region coordinate Y^{3+} in the neighboring molecule in the crystal and thus participate in stabilization of this region. This observation explains why CHP2/NHE1-peptide was crystallized only in the presence of Y^{3+}. These findings suggest that the CHP-unique region is very flexible in aqueous solution. This is consistent with the finding that this region was not seen in the structure of NHE-free CHP1 (Naoe *et al*, 2005), which was solved in different crystal packing.

Interaction between CHP2 and its binding domain in NHE1

Structure determination of the complex revealed the orientation of CHP2 toward the cytoplasmic region of NHE1. The N- and C-terminal halves of the cytoplasmic α-helix of NHE1 are inserted into the hydrophobic cleft in such a way that they face the C- and N-lobes of CHP2, respectively (Figure 3A). This cleft constitutes the region that traps the cytoplasmic α-helix of NHE1 and maintains the stability of the complex by means of hydrophobic interactions. The contact area between CHP2- and NHE1 peptide is 1466 $Å^2$, which accounts for 13.0

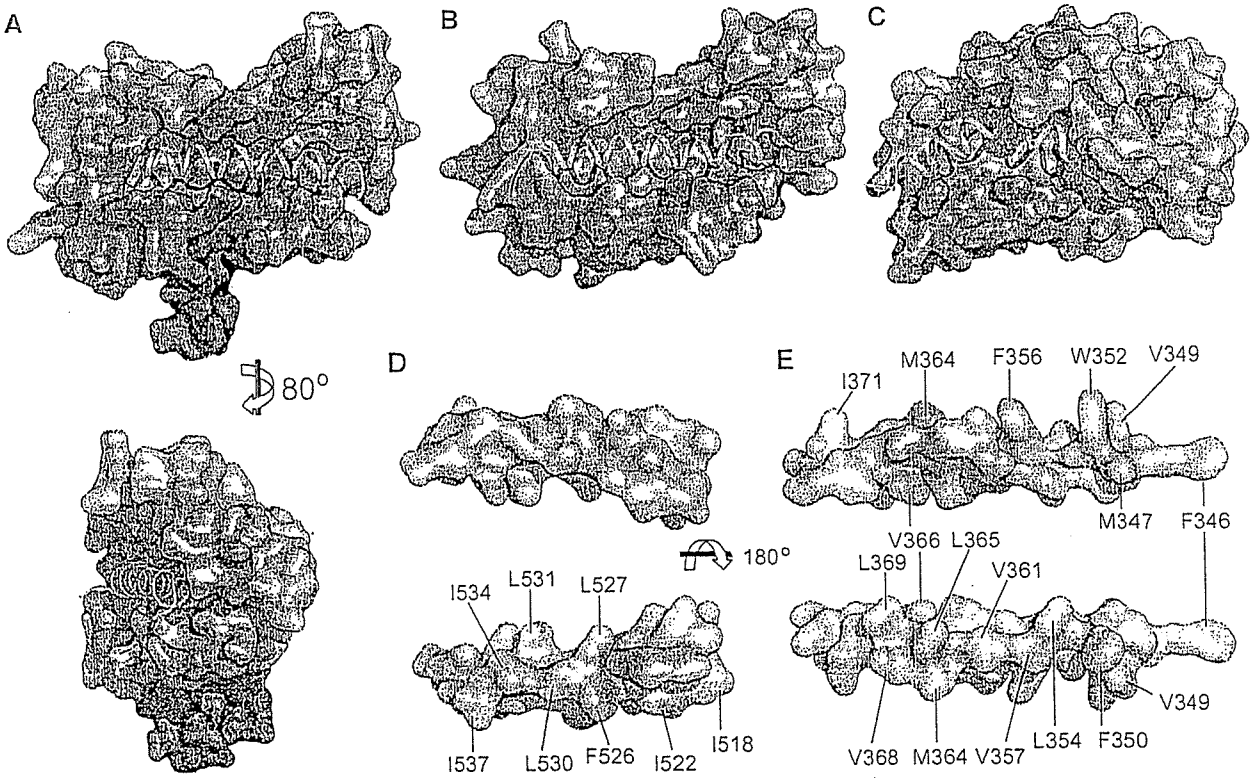

Figure 3 Target specificity of hydrophobic cleft. (A–C) Surface features of CHP2, CNB, and KChP1 are presented together with α-helices of target peptides, respectively. In CHP2, front (*upper*) and side (*lower*) views are shown. The N- and C-lobes are colored *light blue* and *light green*, while the CHP-unique region is colored *red*. (D, E) Surface view of NHE1 (*left*) and CNA (*right*) peptides, respectively. The *upper* panels indicate the side facing outside the cleft and the *lower* panels represent the side facing the cleft. Hydrophobic residues are colored *yellow*.

and 59.8% of the total surface areas, respectively, implying that a large area is used for interaction between the two molecules. The NHE1 peptide (Arg516–His540) solved in this structure contains different hydrophobic residues, all of which face toward the hydrophobic cleft of CHP2 (Figure 3D). Ile518, Ile522, Phe526, Leu527, and Leu530 are accommodated into the cavity formed by hydrophobic residues provided mainly from the C-lobe of CHP2, whereas Leu531, Ile534, and Ile537 are inserted into the cavity formed mainly by the N-lobe of CHP2 (Figure 4A and B). All hydrophobic side chains of the NHE1 peptide, with the exception of Ile518, make van der Waals contacts with side chain atoms from many hydrophobic residues of CHP2. For example, side chain atoms of Ile534 make van der Waals contacts with those of Leu57, Ile66, Phe70, Val86, Leu87 Phe90, Tyr118, and Ile192 of CHP2 (Figure 4C), while side chain atoms of Leu527 make interactions with those of Ala119, Leu181, Val186, Met184, and Met190 (Figure 4A). In addition to hydrophobic interactions, hydrogen bonds strengthen the association between CHP2 and NHE1 peptide. In the N-lobe of CHP2, the guanidinium group of Arg30 makes hydrogen bonds with the main chain carbonyl oxygen of Gly539, while the guanidinium group of Arg34 makes hydrogen bonds with the main chain carbonyl oxygens of Asp536 and Ile537 (Figure 4B). These hydrogen bonds are very important for the C-terminal end of the NHE1 helix to fix to the edge of the hydrophobic cleft of CHP2. The conserved Gly539 residue of NHE1 would allow the following cytoplasmic stretch to leave the cleft by inducing clear bending of the NHE1 peptide (Figures 3A and 4B). Several other hydrogen bonds are also formed. The hydrogen bond between the imidazole group (Nδ) of His523 in NHE1 and the side chain oxygen of Tyr123 in CHP2 is particularly interesting because it is the only polar interaction in the hydrophobic surface of the cleft (Supplementary Figure 3). These polar interactions are important to determine the specificity and orientation of CHP2 toward the cytoplasmic α-helix of NHE1.

Although CNB and KChIP1 have similar hydrophobic clefts (Figure 3B and C), their size and shape are clearly different from those of CHP2. Interestingly, target peptides show sequence features that just fit to their clefts. While NHE1 peptide shows a uniform distribution of hydrophobic residues all facing toward the cleft of CHP2 (Figure 3D), CNA contains more hydrophobic residues that face toward both the CNB crevice and the outside (Figure 3E). In addition, CNA peptide contains four aromatic residues (Phe346, Phe350, Trp352, and Phe356) in the N-terminus, which are accommodated in corresponding hydrophobic cavities in the C-lobe of CNB, whereas NHE1-peptide contains only one aromatic residue (Phe526) located in the central part of CHP2. These observations suggest that highly selective fitting of each peptide to its corresponding crevices may be caused by differences in the distribution of hydrophobic residues of the target peptides and in the shape of the cleft formed by α-helices of EF-hands.

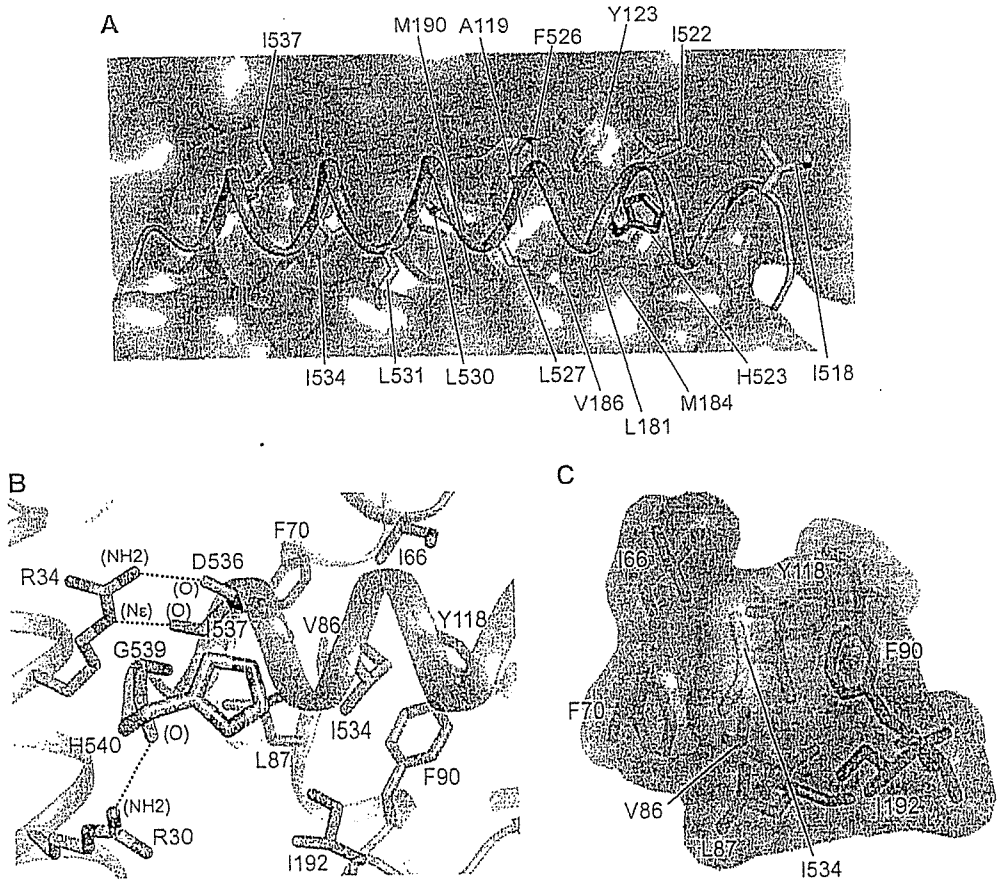

Figure 4 Closeup view showing the interaction between CHP2 and NHE1-peptide. (A) The NHE1-peptide backbone is shown in *magenta*, while hydrophobic side chains are shown in *yellow*. The hydrophobic pocket surrounding Leu527 is marked in *red*. His523 of NHE1 and Tyr123 of CHP2 are marked in *blue*. (B) Closeup view showing interaction between the N-lobe of CHP2 and the C-terminus of NHE1-peptide. (C) Ile534 is accommodated into the hydrophobic pocket produced by residues mainly in the N-lobe of CHP2.

Effect of mutations on interaction between NHE1 and CHP2 in cells

The present structure indicated that the correct CHP-binding domain of NHE1 consists of the region from aa 516–540, extended by 10 residues toward the C-terminus of the region (aa 510–530), as predicted previously (Pang *et al*, 2001). This prompted us to mutate residues in this extended region of NHE1 interacting with the N-lobe of CHP2. We mutated the Ile534 and Ile537 residues of NHE1 into charged residues (Lys or Asp) and stably expressed these mutants in exchanger-deficient PS120 cells. These mutants were expressed in the plasma membrane (as indicated by the existence of surface-expressed mature NHE1 in Supplementary Figure 4). We examined the interactions of these mutants with CHP2 by assessing whether stably transfected green fluorescent protein (GFP)-tagged CHP2 was localized to the plasma membrane. As shown in Figure 5A, most of the CHP2 was localized to the plasma membrane of cells expressing the wild-type NHE1 but not in nontransfected PS120 cells (not shown; see Pang *et al*, 2001), indicating a strong interaction. Of note, in most cells expressing the wild-type NHE1 almost no GFP-fluorescence was detected in the intracellular space (Figure 5A), despite the accumulation of immature NHE1 in the intracellular membranes under forced expression (data not shown), suggesting that CHP2 interacts predominantly with mature NHE1 in the plasma membrane. This was further confirmed by the finding that almost no immature NHE1 co-immunoprecipitated with CHP2 (Supplementary Figures 1 and 4). In contrast to the wild-type NHE1, the plasma membrane localization of CHP2 was almost completely abolished when transfected into cells expressing the NHE1 mutants, I534K, I534D and I537K (Figure 5, and also D for summarized data), indicating that these mutations drastically reduced the affinity for interaction with CHP2.

Furthermore, as expected, the plasma membrane localization of CHP2 was also markedly reduced in cells expressing the wild-type NHE1 when Leu87 or Tyr118 of CHP2 was changed to Lys (Figure 5C and D), indicating that these mutants are not able to replace completely endogenous CHP1 bound to NHE1. As the expression of GFP-tagged CHP2 was approximately 10-fold higher than that of endogenous CHP1 (data not shown), these results suggest that these mutations would reduce the affinity for interaction with NHE1 at least one-order of magnitude. Similar analysis was performed with mutation of the Arg residues (Arg30 and Arg34) in the N-terminal α-helix of CHP2. The plasma membrane localization of CHP2 was abolished when these two residues were simultaneously changed to Glu (Figure 5C and D), while it was still partially preserved when either Arg residue alone was changed to Glu. Similar results were also obtained for the NHE1/CHP2 interaction in a co-immunoprecipitation experiment (Supplementary Figure 4). Thus, the hydrophobic and polar interactions involving these residues would be important in determining the strong and highly specific association between NHE1 and CHP2, Furthermore, in addition to the C-lobe, the N-lobe of CHP2 plays a crucial role in the tight interaction with NHE1, suggesting that our crystal structure reflects the interaction between native NHE1 and CHP2 molecules expressed in cells. On the other hand, structure determination indicated the existence of a unique protruding region in CHP2. In contrast to mutations of residues involving formation of the cleft, a mutant with deletion of this CHP-unique region (Δ94–104) was mostly localized to the plasma membrane of cells expressing wild-type NHE1 (Figure 5C), indicating that deletion did not disrupt the interaction of CHP2/NHE1. Hence, as also predicted from structure, the CHP-unique region was not involved in the interaction between CHP2/NHE1. The 10 N-terminal residues of CHP2 were also found not to be involved in the interaction, as indicated by the plasma membrane localization of ΔN10 (Figure 5C).

Functional consequence of mutations

We measured the NHE activity in cells expressing mutant exchangers. Figure 6A demonstrates the pH_i-dependence of EIPA-sensitive $^{22}Na^+$-uptake activity. While the wild-type NHE1 exhibited high $^{22}Na^+$-uptake activity, with pK ~6.5 for pH_i (Hill coefficient, ~1.7), the activity of mutant exchangers, I534D, I534K and Ile537, which lack CHP-binding was very low (see Supplementary Table I for kinetic parameters). The inhibitory effect of the mutations was characterized by changes in two parameters: (i) a drastic reduction of maximal $^{22}Na^+$-uptake activity (V_{max}) at acidic pH_i, and (ii) a large acidic shift of the pH_i-dependence of uptake (>0.6 pH units) (see Figure 6A, inset for normalized activity). We then compared the pH_i-dependence of $^{22}Na^+$-uptake in cells co-expressing NHE1 with GFP-tagged CHP2 or its deletion mutant Δ94–104, which preserves interaction with CHP. Interestingly, expression of Δ94–104 significantly shifted the pH_i-dependence of uptake towards acidic pH_i (~0.2 pH unit) without any change in V_{max}, while it preserved the cooperative pH_i dependence, with a Hill coefficient ~1.5 (Figure 6B, see also inset for the sigmoidal internal H^+ dependence), suggesting that the CHP-unique region is involved in regulation of pH-sensing of NHE1. In general, the sigmoidal H^+-dependence has been interpreted as exhibiting involvement of at least two H^+-binding sites: H^+-transport and H^+-regulatory sites in NHE (Wakabayashi *et al*, 1997). To examine the effect of deletion of a CHP-specific region on the H^+-regulatory site, we measured the reverse reaction of NHE1, that is, $^{22}Na^+$ efflux coupled to H^+-influx. If we assume that NHE1 catalyzes a counter-transport reaction only involving the transport site, intracellular acidification should result in inhibition of $^{22}Na^+$ efflux due to cytosolic Na^+/H^+ competition. In contrast to this thermodynamically expected inhibition, modest acidification from 7.5 to 7.2 dramatically stimulated the rate of EIPA-inhibitable $^{22}Na^+$ efflux in cells co-expressing the wild-type NHE1 and CHP2 (Figure 6D), suggesting that protonation of H^+-regulatory sites activated NHE1 (Figure 6C), as reported in detail, previously (Aronson *et al*, 1982; Wakabayashi *et al*, 2003a). Consistent with the acidic shift of pH_i-dependence of $^{22}Na^+$ uptake, we observed that deletion of a CHP-unique region significantly reduced the rate of $^{22}Na^+$ efflux (Figure 6D). EIPA-sensitive fraction of $^{22}Na^+$ efflux at pH_i 7.2 during the initial 3 min was reduced to ~30% upon expression of Δ94–104, suggesting that the affinity of the H^+-regulatory site for H^+ decreased upon deletion of this region.

Discussion

In the present study, we solved the first crystal structure of the CHP2/NHE1-peptide complex at 2.7 Å. This structure provides detailed information regarding the interaction between

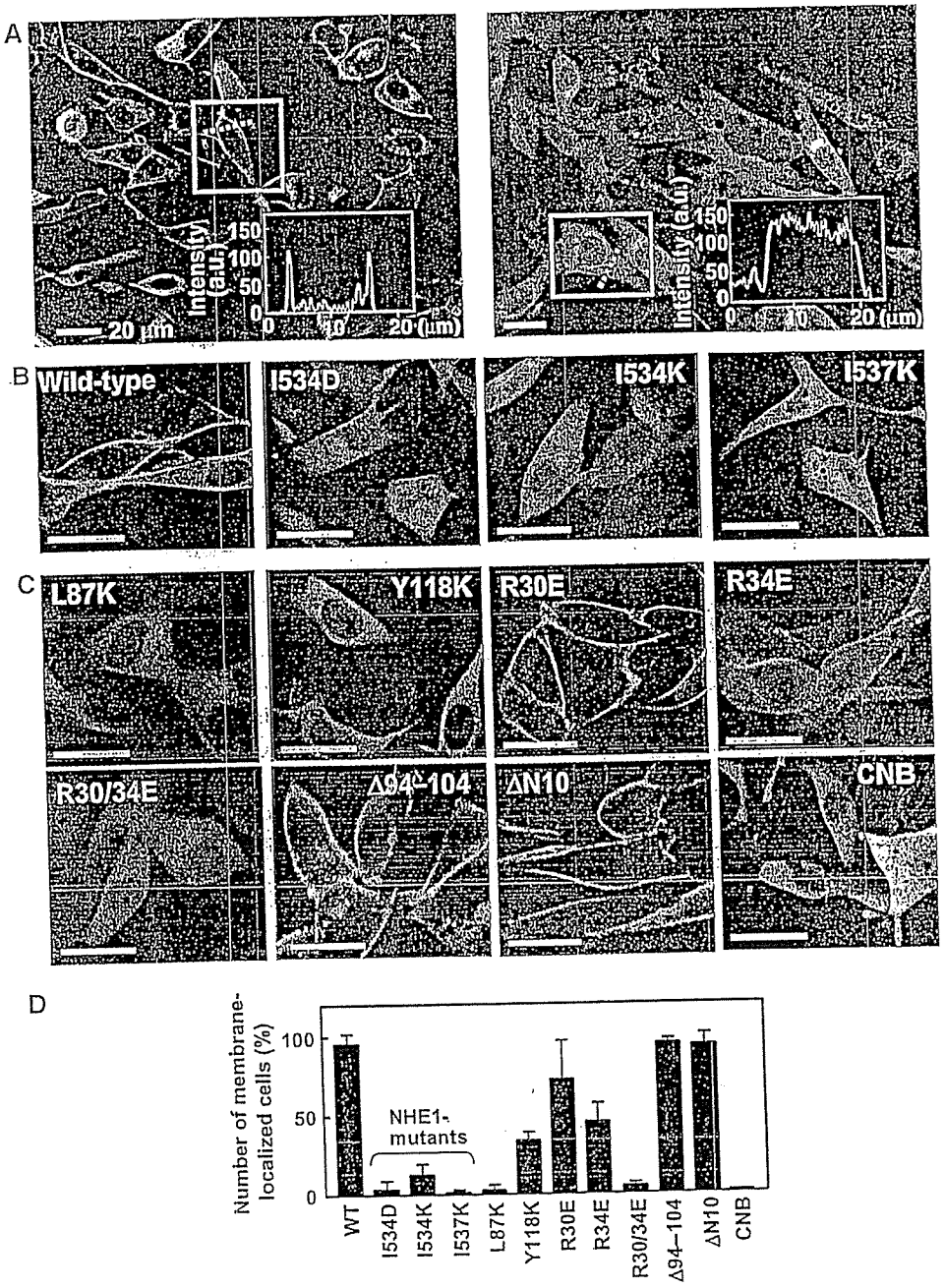

Figure 5 Effects of mutations on the interaction between NHE1 and CHP2 in cells. (A) Low magnification confocal images of cells coexpressing GFP-tagged CHP2 and the wild-type (*left*) or I537K (*right*) mutant exchangers. Inset shows the intensity profile of GFP fluorescence along the dotted line in a marked cell. In most cells expressing the wild-type NHE1 but not I537K, strong fluorescent signals were detected at the cell edge. (B) Subcellular localization of CHP2 expressed in cells. GFP-tagged CHP2 was coexpressed in cells stably expressing the wild-type or mutant NHE1 variants and GFP-fluorescence was observed by confocal microscopy. (C) Subcellular localization of mutant CHP2. GFP-tagged CHP2 mutants were expressed in cells stably expressing the wild-type NHE1. Eleven residues from Glu94 to Lys104 of CHP2 were deleted in Δ94–104, while the 10 N-terminal residues from Met1 to Val10 were deleted in ΔN10. For one control experiment, GFP-tagged human CNB was expressed in NHE1-transfectants. (D) Summary data for membrane localization of GFP-tagged CHP2. Intensity profile analysis was performed on confocal images as shown in (A). The number of cells with strong fluorescence signal at the cell edge (at least three times more than the average of fluorescence in the internal cell region) was counted. Data are expressed as the mean±s.d. from 6–8 images (total cell number analyzed, 99–341).

NHE1 and CHP: (i) the interaction with NHE1 occurs in a hydrophobic cleft encompassing the N- and C-lobes of CHP2, (ii) this interaction occurs by extensive Van der Waals contact between hydrophobic residues, as well as by some specific hydrogen bonds, (iii) the interacting region of NHE1 forms an α-helix which bends at a conserved Gly539 and (iv) two domains of CHP2 are connected by a large flexible CHP-unique region. These features strengthened our previous functional study (Pang *et al*, 2001, 2002, 2004) from structural aspects and at the same time provided new information to be addressed regarding the function of NHE1.

A unique feature of interaction between CHP and NHE

Structure comparison among Ca^{2+}-binding proteins provided valuable information regarding the target specificity of CHP1/2 proteins. Although the crystal structure of CNB/CNA com-

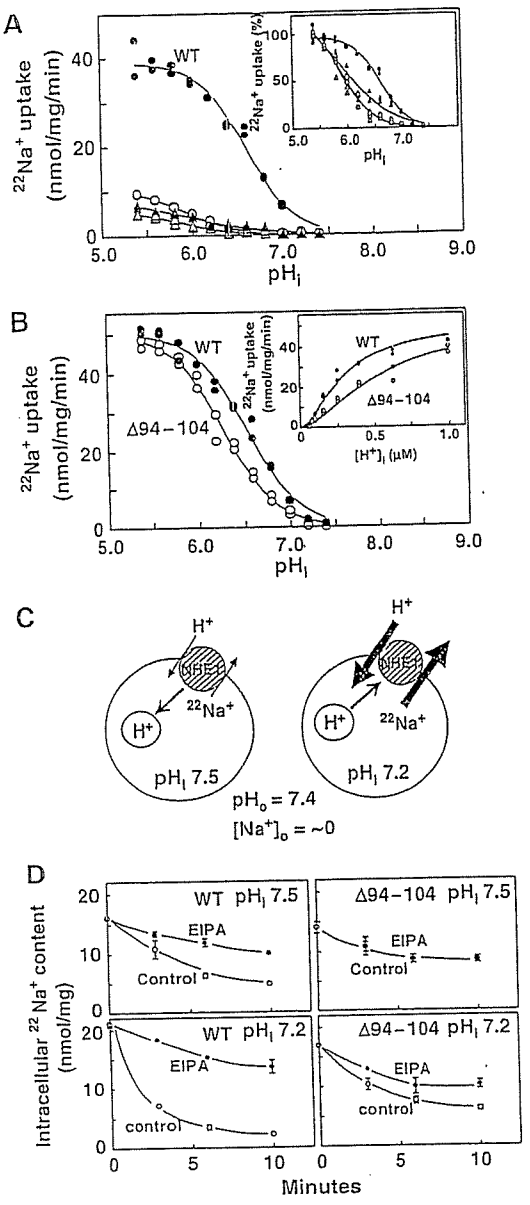

Figure 6 Effect of mutations on the exchange activity. (A), pH$_i$-dependence of EIPA-sensitive $^{22}Na^+$-uptake in cells expressing wild-type NHE1 (●) or CHP binding-defective mutants, I534D (○), I534K (▲) and I537K (△). pH$_i$ was clamped at various values with K^+/nigericin. Data were fitted to Hill equations with the kinetic parameters shown in Supplementary Table I and plotted after normalization by the maximal activity at pH$_i$ = 5.4 (*inset*). (B) pH$_i$-dependence of EIPA-sensitive $^{22}Na^+$-uptake in cells co-expressing wild-type NHE1 and GFP-tagged CHP2 (●) or deletion mutant Δ94–104 of CHP2 (○). Data were fitted to Hill equations with the kinetic parameters shown in Supplementary Table I. The $^{22}Na^+$-uptake activity was also plotted against intracellular H^+ concentration up to 1 μM (*inset*). (C) Schematic drawing of $^{22}Na^+$-efflux protocol. The efflux experiment was done in $^{22}Na^+$-loaded, pH$_i$-clamped cells at extracellular pH 7.4. At lower pH$_i$ $^{22}Na^+$ efflux would be accelerated by H^+ binding to the regulatory site, while at high pH$_i$ it would be inhibited by H^+-release from the regulatory site. (D) Time courses of $^{22}Na^+$ efflux. Cells were loaded with $^{22}Na^+$ and at the same time pH$_i$-clamped at pH$_i$ 7.5 or 7.2. After removal of the radioactive solution, cells were exposed to the nonradioactive solutions with or without 0.1 mM EIPA. Data are expressed as the mean ± s.d. of three determinations. Error bars are sometimes smaller than symbol sizes.

plex (Kissinger *et al*, 1995) revealed a similar mode of interaction through its hydrophobic groove, comparison between the hydrophobic clefts of CHP2 and CNB showed several different structural features (Figure 3A and B). In addition, there is a marked difference in the distribution of hydrophobic residues between NHE1- and CNA peptides (Figure 3D and E). Such local structural differences between CHP2 and CNB, together with differences between target peptide sequences, may explain the selectivity of CHP1/2 toward the NHE members and of CNB toward CNA, and led us to predict that NHE1 may not be a target for CNB. In fact, we observed that GFP-tagged CNB was not localized to the plasma membrane when co-expressed with NHE1 (Figure 5C). On the other hand, since the C-lobe of KChIP1 is occupied by the α10 helix of itself (Figure 3C), KChIP1 associates with its target K^+-channel molecule only through the N-lobe (Zhou *et al*, 2004). Crystal structures have been also solved for several other Ca^{2+}-binding proteins belonging to the NCS family: recoverin (Flaherty *et al*, 1993), NCS-1 (Bourne *et al*, 2001), neurocalcin (Vijay-Kumar and Kumar, 1999), AtCBL2 (Nagae *et al*, 2003), and CIB (Gentry *et al*, 2005). Although all these proteins have hydrophobic crevices that would interact with the target molecules, the sizes and shapes of these crevices are clearly different. In contrast to calmodulin, which is able to interact with a variety of proteins with broad specificity, target molecules for CNB and NCS family proteins appear to be limited. Structural differences in the hydrophobic cleft together with highly specific polar interactions would enable the diverse array of Ca^{2+} binding proteins belonging to these families to associate selectively and tightly with the target molecules.

Of note, the N-lobe of CHP2 associates tightly with the C-lobe within a large area (Figure 3A). The contact area between the two domains is 1066 Å^2, accounting for 16.6 and 15.2% of the total surface areas of the N- and C-lobes, respectively. Such interaction between the two lobes would result in the formation of a rigid cleft structure independent of the target peptide. In fact, the structure of the hydrophobic cleft of CHP2 is very similar to that of target-free CHP1 (Naoe *et al*, 2005). In addition, the N-lobe of CHP2 does not contain the methionine residue that was suggested to produce plasticity allowing fine-tuning toward various target molecules in calmodulin (Osawa *et al*, 1998). Therefore, NHE1-peptide would enter the preformed cleft, rather than the interaction being caused by a conformational change in the cleft. This target-independent rigid structure would allow the CHP-unique region to exert specific physiological functions, beyond a role as a connecting linker. This is in contrast to calmodulin the flexible liker region between the two domains of which is known to act as a hinge when it recognizes various target molecules (Zhang *et al*, 1995).

CHP1/2 is myristoylated and has two Ca^{2+} ions. However, these properties are different from those of other CNB and NCS family proteins. Mutation of CHP1 that prevents myristoylation has no apparent effect on plasma membrane expression or the exchange activity of NHE1. Therefore, myristoylation of CHP1/2 would not be required for the plasma membrane translocation of NHE1 or for the exchange activity (Pang *et al*, 2001, 2004), in contrast to KChIP1 (An *et al*, 2000). In addition, unlike recoverin, which undergoes the Ca^{2+}-myristoyl switch (Ames *et al*, 1997), the myristoyl moiety of CHP1/2 would always be exposed outside the core structure upon interaction with NHE1 and probably embedded in the plasma membrane. Thus, the physiological function of myristoylation is still unknown. On the other hand,

unlike many other Ca^{2+}-binding proteins, only EF3 and EF4 of CHP1/2 are able to coordinate Ca^{2+} ions. Removal of Ca^{2+} with a Ca^{2+}-chelator significantly reduced the interaction between NHE1 and CHP2 (Supplementary Figure 1) and a double mutation of EF3 and EF4 of CHP1 abolished the interaction with NHE1 (Pang *et al*, 2004). Furthermore, the Ca^{2+} affinity of CHP1 increases markedly (40-fold) upon interaction with NHE1 (Pang *et al*, 2004). These findings suggest that Ca^{2+}-binding sites and the hydrophobic cleft are structurally coupled, that is, the Ca^{2+}-bound conformation of EF-hands is required for the formation of the appropriate structure of the hydrophobic cleft for the interaction with NHE1. By analogy with calmodulin (Zhang *et al*, 1995), we consider that Ca^{2+} binding opens the hydrophobic pockets of EF-hands so that the residues of the C-lobe can fit into the hydrophobic cleft. However, such Ca^{2+}-induced conformational changes of CHP1/2 bound to NHE1 would not occur physiologically in cells, since the Ca^{2+} affinity for such a complex would be extremely high, that is, K_d for Ca^{2+} ($2\sim3$ nM) is much less than the physiological cytosolic Ca^{2+} concentration (0.1–1 μM) (Supplementary Figure 1 and see also Pang *et al*, 2004). Hence, we suggest that Ca^{2+} bound to EF-hands plays a structural role in stabilizing the hydrophobic cleft of CHP1/2. In the case of NHE1, Ca^{2+}-induced activation would take place on another Ca^{2+}-binding protein CaM, which binds to the middle of the cytoplasmic domain of NHE1 (Bertrand *et al*, 1994; Wakabayashi *et al*, 1994).

Implications for roles of CHP in NHE function

We demonstrated that Ile534 and Ile537 in NHE1 are critical residues for interaction with CHP2 (Figure 5). Mutations of these residues resulted in a disruption of NHE1 function, as characterized by a drastic reduction of the maximal exchange activity and a large acidic shift of the pH_i-dependence of exchange (Figure 6). This is consistent with our previous findings obtained by simultaneous mutation of four hydrophobic residues (Phe526, Leu527, Leu530 and Leu531) of NHE1, substituted with Gln or Arg (Pang *et al*, 2001, 2004). On the other hand, deletion of the CHP-unique region (Δ94–104) significantly reduced the physiological exchange activity by inducing an acidic shift of the pH_i-dependence of $^{22}Na^+$-uptake (Figure 6B) and inhibited the rate of $^{22}Na^+$ efflux (Figure 6D), while preserving the maximal activity at acidic pH_i (Figure 6B), suggesting that this region functions as an important segment controlling pH_i by interacting with NHE1. Based on these findings, we propose that CHP1/2 plays two important roles in the function of NHE1. First, CHP functions as an obligatory subunit, which activates almost non-functional NHE1 by tightly associating with its cytoplasmic domain via the hydrophobic cleft. This activation is characterized by increases in both V_{max} and the H^+-affinity. Secondly, CHP would participate in the delicate pH_i regulation of NHE1 through the CHP-unique region, which is involved in modulation of the H^+-affinity, but not V_{max}.

We predict that CHP may stabilize the structure of the juxtamembrane domain by inducing a stable α-helix, thereby preserving NHE1 in the functional conformation. Indeed, circular dichroism measurements indicated that the CHP-free, CHP-binding peptide has no secondary structure in aqueous solution (data not shown), although we do not exclude the possibility that this region is folded within the entire structure. On the other hand, the dominant-negative effect of Δ94–104 raises the interesting possibility that it may regulate the pH_i-sensing by interacting with some regions of NHE1. We observed that NHE1 and CHP2 crosslinked with each other through IL5 of NHE1 and the CHP-unique region (Supplementary Figure 5), suggesting that these regions in the two proteins are located in accessible positions beneath the membranes. Since, similar to Δ94–104 of CHP2, mutation of Arg440 in IL5 results in a large acidic shift of the pH_i-dependence of $^{22}Na^+$-uptake and efflux (Wakabayashi *et al*, 2003a, b), we consider that IL5 would be one of targets for the CHP-unique region. Although we do not have direct evidence, IL4 may be another target region because mutation of Arg327 in IL4 has also been reported to lead to a similar functional defect of NHE1(Lacroix *et al*, 2004). Activation of $^{22}Na^+$ efflux by cytosolic acidification predicted the existence of an additional H^+-regulatory site(s) (Figure 6C and D; Aronson *et al*, 1982; Wakabayashi *et al*, 2003a). This phenomenon does not appear to be fully explained by the recent allosteric model, in which only H^+-transport sites are assumed to participate in the cooperative H^+-activation of NHE1 (Lacroix *et al*, 2004). We speculate that multiple charged residues in loops of NHE1, as well as in CHP1/2, may serve as 'pH-sensor' sites, which accept protons, although further investigation will be required to support this concept. The recently reported crystal structure of the bacterial Na^+/H^+ antiporter, NhaA, predicted that modification of charged residues provided by cytoplasmic loops may activate NhaA by exposing the cation transport site via reorientation of transmembrane helices (Hunte *et al*, 2005).

Finally, it should be noted that the relatively long juxtamembrane domain (aa 503–595) of NHE1 is essential for the physiological exchange activity (Ikeda *et al*, 1997; Wakabayashi *et al*, 1997), although we focused on the CHP-binding domain in the present study. Similar to the CHP-binding region, it is likely that the region covering aa 503–595 forms a stable structure by interacting with several accessory factors. Indeed, this region appears to be structurally unstable when expressed in *Escherichia coli* or in mammalian cells as a single polypeptide, as evidenced by its rapid degradation (unpublished observation), despite the fact that the whole cytoplasmic domain can be easily expressed in these cells. In addition, a previous study (Aharonovitz *et al*, 2000) indicated that positively charged clusters (aa 509–516 and aa 552–560 in human NHE1) interact with polyphosphoinosides (PIP_2). These regions were also reported to interact with ezrin, although interaction with ezrin is independent of the exchange activity (Denker *et al*, 2000; Baumgartner *et al*, 2004). Furthermore, we recently reported that a region (aa 560–580) of NHE1 may be involved in dimeric interactions (Hisamitsu *et al*, 2004). Such homotypic interactions may provide another way for stabilization of the structure, as deletion of aa 560–580 resulted in a marked reduction of exchange activity by inducing the acidic shift of pH_i-dependence (Hisamitsu *et al*, 2004). These findings raise the possibility that multiple homotypic and heterotypic interactions may induce stabilization of the juxtamembrane region and thereby form a substructure regulating the exchange activity. Clearly, CHP is an obligatory member in such regulatory machinery of NHE1.

In summary, we first determined the crystal structure of CHP2 complexed with its binding region in NHE1 and

clarified the mechanism by which CHP tightly and specifically associates with plasma membrane members of the NHE family. Structure-based mutagenesis revealed the physiological importance of CHP in pH_i regulation by NHE1. Most Ca^{2+}-binding proteins have long been recognized to function as Ca^{2+}-sensors or Ca^{2+}-buffers. In contrast to this general understanding, CHP does not appear to be a Ca^{2+}-sensor, but rather acts as a critical regulator of pH-sensing activity in the exchangers, presumably mediated by the CHP-unique region. The results of the present study cast new light on a unique function of CHP that was not reported in other canonical EF-hand Ca^{2+}-binding proteins.

Materials and methods

Protein expression and purification

The complex of human full-length CHP2 (aa 1–196) with its binding region (aa 503–545) in NHE1 was expressed and purified essentially as described previously (Pang *et al*, 2004; Ben Ammar *et al*, 2005).

Crystallization and data collection

Crystals of the complex CHP2/NHE1-peptide were grown using the sitting-drop vapor diffusion technique at 20°C. To obtain the best crystal quality, 1.5 µl of the protein complex solution containing 20 mM yttrium chloride was mixed with 1 µl of the reservoir solution containing 200 mM ammonium acetate, 100 mM Bis–Tris, pH 5.5, and 25% (w/v) PEG 3350 as described previously (Ben Ammar *et al*, 2005). Crystals were not obtained without adding yttrium chloride to the crystallization solution, suggesting that yttrium ion(s) were involved in crystal packing. Therefore, taking advantage of the yttrium ion(s) in the crystal, we collected multiple wavelength data sets around the absorption edge of the yttrium atom at SPring-8 beamline BL44B2. A high-resolution single-wavelength data set ($\lambda = 1$ Å) was collected at beamline BL41XU at SPring-8. The statistics of the data collection are summarized in Table I.

Structural determination and refinement

The structure of the CHP2/NHE1-peptide complex was determined by MAD phasing. The program SOLVE (Terwilliger and Berendzen, 1999) was used to determine two yttrium positions and the initial phases with a figure of merit of 0.43 at 3.1 Å resolution. The program RESOLVE (Terwilliger, 2000) improved the phases and produced the initial polyalanine model, which covered 65% of the residues of the CHP2/NHE1-peptide complex. The model was built with TURBO-FRODO and refined against the high resolution data set to 2.7 Å using CNS (Brunger *et al*, 1998), and subsequent rounds of model building and refinement produced the final structural model. The residues in the final model lie in 87.2% in the most favorable and 12.8% in the additionally allowed regions of the Ramachandran plot. Refinement statistics are summarized in Table I. Figures 2–4 were generated using PyMOL graphing software (http://www.pymol.org).

Construction of mammalian expression plasmids

The plasmid carrying the cDNA encoding NHE1 containing unique restriction sites cloned into the mammalian expression vector pECE was described previously (Wakabayashi *et al*, 1992). Construction of plasmids for various NHE1 or CHP2 mutants tagged with GFP or hemagglutinin (HA) epitope YPYDVPDYAS was carried out by a PCR-based strategy as described previously (Wakabayashi *et al*, 2000). PCR fragments were digested and cloned into the appropriate restriction sites of vectors pECE or pGEFP-N1 (Clontech, Palo Alto, CA) for NHE1 or CHP2, respectively.

Cell culture and plasmid transfection

The exchanger-deficient cell line PS120 (Pouyssegur *et al*, 1984) and corresponding transfectants were maintained in Dulbecco's modified Eagle's medium containing 25 mM $NaHCO_3$ and supplemented with 5% (v/v) fetal calf serum. All cDNA constructs were transfected into PS120 cells with Lipofectamine 2000 (Invitrogen), and stable clones for NHE1 and its mutant constructs were selected by repetitive H^+-killing selection procedures as described previously (Wakabayashi *et al*, 1992). GFP-tagged CHP2 variants were stably expressed in cells expressing various mutant NHE1 proteins and fluorescence images were taken under a confocal fluorescence microscope (BioRad).

Measurement of $^{22}Na^+$-uptake and $^{22}Na^+$-efflux activities

$^{22}Na^+$-uptake activity was measured by the K^+/nigericin pH_i clamp method as described previously (Ikeda *et al*, 1997). Data were simulated by fitting the values to the sigmoidal dose–response equation, rate of EIPA-sensitive $^{22}Na^+$-uptake $= V_{max}/(1 + 10^{(\log(pK - pH_i)^n)})$ (pK, pH_i giving half maximal $^{22}Na^+$ uptake; n, Hill coefficient), using the simulation program included in Graphpad Prizm (Microsoft Corp., Redmond, WA). $^{22}Na^+$ efflux was measured as described previously (Wakabayashi *et al*, 2003a). Briefly, serum-depleted cells in 24-well dishes were loaded with $^{22}Na^+$ by preincubating them for 30 min at 37°C in chloride/KCl medium containing 1 mM $^{22}NaCl$ (37 kBq/ml) and at the same time pH_i-clamped at 7.5 or 7.2 in presence of 5 µM nigericin. The radioactive solution was removed and $^{22}Na^+$ efflux was initiated by adding the nonradioactive medium. At the times indicated in figures, cells were rapidly washed four times with ice-cold PBS and the remaining ^{22}Na-radioactivity in the cells was counted.

Coordinates

Coordinates and structure factor amplitudes have been deposited in the Protein Data Bank with accession code 2BEC.

Supplementary data

Supplementary data are available at *The EMBO Journal* Online.

Acknowledgements

We thank the staff at beamline BL44B2 and BL41XU, SPring-8, for support with data collection, Dr Sugawara and Dr Miyano (RIKEN Harima Institute) for fruitful discussion, Dr Tomoe Y Nakamura for critical reading of manuscript, and Dr Tianxiang Pang for the initial participation in this study. This work was supported by Grant nano-001 for Research on Advanced Medical Technology from the Ministry of Health, Labor, and Welfare of Japan and Grant-in-Aid for Priority Areas 13142210 for Scientific Research from the Ministry of Education, Science, and Culture of Japan. YBA is a Japan Society for the Promotion of Science (JSPS) Postdoctoral Fellow.

References

Aharonovitz O, Zaun HC, Balla T, York JD, Orlowski J, Grinstein S (2000) Intracellular pH regulation by Na(+)/H(+) exchange requires phosphatidylinositol 4,5-bisphosphate. *J Cell Biol* 150: 213–224

Ames JB, Ishima R, Tanaka T, Gordon JI, Stryer L, Ikura M (1997) Molecular mechanics of calcium-myristoyl switches. *Nature* 389: 198–202

An WF, Bowlby MR, Betty M, Cao J, Ling HP, Mendoza G, Hinson JW, Mattsson KI, Strassle BW, Trimmer JS, Rhodes KJ (2000) Modulation of A-type potassium channels by a family of calcium sensors. *Nature* 403: 553–556

Aronson PS, Nee J, Suhm MA (1982) Modifier role of internal H+ in activating the Na+-H+ exchanger in renal microvillus membrane vesicles. *Nature* 299: 161–163

Barroso MR, Bernd KK, DeWitt ND, Chang A, Mills K, Sztul ES (1996) A novel Ca2+-binding protein, p22, is required for constitutive membrane traffic. *J Biol Chem* 271: 10183–10187

Baumgartner M, Patel H, Barber DL (2004) Na(+)/H(+) exchanger NHE1 as plasma membrane scaffold in the assembly of signaling complexes. *Am J Physiol Cell Physiol* 287: C844–C850

Ben Ammar Y, Takeda S, Sugawara M, Miyano M, Mori H, Wakabayashi S (2005) Crystallization and preliminary crystal-

lographic analysis of the human calcineurin homologous protein CHP2 bound to the cytoplasmic region of the Na+/H+ exchanger NHE1. *Acta Crystallograph Sect F* 61: 956–958

Bertrand B, Wakabayashi S, Ikeda T, Pouyssegur J, Shigekawa M (1994) The Na+/H+ exchanger isoform 1 (NHE1) is a novel member of the calmodulin-binding proteins. Identification and characterization of calmodulin-binding sites. *J Biol Chem* 269: 13703–13709

Bourne Y, Dannenberg J, Pollmann V, Marchot P, Pongs O (2001) Immunocytochemical localization and crystal structure of human frequenin (neuronal calcium sensor 1). *J Biol Chem* 276: 11949–11955

Brunger AT, Adams PD, Clore GM, DeLano WL, Gros P, Grosse-Kunstleve RW, Jiang JS, Kuszewski J, Nilges M, Pannu NS, Read RJ, Rice LM, Simonson T, Warren GL (1998) Crystallography & NMR system: a new software suite for macromolecular structure determination. *Acta Crystallogr D* 54 (Part 5): 905–921

Counillon L, Pouyssegur J (2000) The expanding family of eucaryotic Na(+)/H(+) exchangers. *J Biol Chem* 275: 1–4

Denker SP, Huang DC, Orlowski J, Furthmayr H, Barber DL (2000) Direct binding of the Na–H exchanger NHE1 to ERM proteins regulates the cortical cytoskeleton and cell shape independently of H(+) translocation. *Mol Cell* 6: 1425–1436

Engelhardt S, Hein L, Keller U, Klambt K, Lohse MJ (2002) Inhibition of Na(+)-H(+) exchange prevents hypertrophy, fibrosis, and heart failure in beta(1)-adrenergic receptor transgenic mice. *Circ Res* 90: 814–819

Flaherty KM, Zozulya S, Stryer L, McKay DB (1993) Three-dimensional structure of recoverin, a calcium sensor in vision. *Cell* 75: 709–716

Gentry HR, Singer AU, Betts L, Yang C, Ferrara JD, Sondek J, Parise LV (2005) Structural and biochemical characterization of CIB1 delineates a new family of EF-hand-containing proteins. *J Biol Chem* 280: 8407–8415

Gutierrez-Ford C, Levay K, Gomes AV, Perera EM, Som T, Kim YM, Benovic JL, Berkovitz GD, Slepak VZ (2003) Characterization of tescalcin, a novel EF-hand protein with a single Ca2+-binding site: metal-binding properties, localization in tissues and cells, and effect on calcineurin. *Biochemistry* 42: 14553–14565

Hisamitsu T, Pang T, Shigekawa M, Wakabayashi S (2004) Dimeric interaction between the cytoplasmic domains of the Na+/H+ exchanger NHE1 revealed by symmetrical intermolecular cross-linking and selective co-immunoprecipitation. *Biochemistry* 43: 11135–11143

Hunte C, Screpanti E, Venturi M, Rimon A, Padan E, Michel H (2005) Structure of a Na+/H+ antiporter and insights into mechanism of action and regulation by pH. *Nature* 435: 1197–1202

Ikeda T, Schmitt B, Pouyssegur J, Wakabayashi S, Shigekawa M (1997) Identification of cytoplasmic subdomains that control pH-sensing of the Na+/H+ exchanger (NHE1): pH-maintenance, ATP-sensitive, and flexible loop domains. *J Biochem (Tokyo)* 121: 295–303

Inoue H, Nakamura Y, Nagita M, Takai T, Masuda M, Nakamura N, Kanazawa H (2003) Calcineurin homologous protein isoform 2 (CHP2), Na+/H+ exchangers-binding protein, is expressed in intestinal epithelium. *Biol Pharm Bull* 26: 148–155

Karmazyn M (2001) Role of sodium-hydrogen exchange in cardiac hypertrophy and heart failure: a novel and promising therapeutic target. *Basic Res Cardiol* 96: 325–328

Kissinger CR, Parge HE, Knighton DR, Lewis CT, Pelletier LA, Tempczyk A, Kalish VJ, Tucker KD, Showalter RE, Moomaw EW, Gastinel LN, Habuka N, Chen X, Maldonado F, Barker JE, Bacquet R, Villafranca JE (1995) Crystal structures of human calcineurin and the human FKBP12-FK506-calcineurin complex. *Nature* 378: 641–644

Lacroix J, Poet M, Maehrel C, Counillon L (2004) A mechanism for the activation of the Na/H exchanger NHE-1 by cytoplasmic acidification and mitogens. *EMBO Rep* 5: 91–96

Lin X, Barber DL (1996) A calcineurin homologous protein inhibits GTPase-stimulated Na-H exchange. *Proc Natl Acad Sci USA* 93: 12631–12636

Mailander J, Muller-Esterl W, Dedio J (2001) Human homolog of mouse tescalcin associates with Na(+)/H(+) exchanger type-1. *FEBS Lett* 507: 331–335

Nagae M, Nozawa A, Koizumi N, Sano H, Hashimoto H, Sato M, Shimizu T (2003) The crystal structure of the novel calcium-binding protein AtCBL2 from *Arabidopsis thaliana*. *J Biol Chem* 278: 42240–42246

Naoe Y, Arita K, Hashimoto H, Kanazawa H, Sato M, Shimizu T (2005) Structural characterization of calcineurin B homologous protein 1. *J Biol Chem* 280: 32372–32378

Orlowski J, Grinstein S (2004) Diversity of the mammalian sodium/proton exchanger SLC9 gene family. *Pflugers Arch* 447: 549–565

Osawa M, Swindells MB, Tanikawa J, Tanaka T, Mase T, Furuya T, Ikura M (1998) Solution structure of calmodulin-W-7 complex: the basis of diversity in molecular recognition. *J Mol Biol* 276: 165–176

Pang T, Hisamitsu T, Mori H, Shigekawa M, Wakabayashi S (2004) Role of calcineurin B homologous protein in pH regulation by the Na+/H+ exchanger 1: tightly bound Ca2+ ions as important structural elements. *Biochemistry* 43: 3628–3636

Pang T, Su X, Wakabayashi S, Shigekawa M (2001) Calcineurin homologous protein as an essential cofactor for Na+/H+ exchangers. *J Biol Chem* 276: 17367–17372

Pang T, Wakabayashi S, Shigekawa M (2002) Expression of calcineurin B homologous protein 2 protects serum deprivation-induced cell death by serum-independent activation of Na+/H+ exchanger. *J Biol Chem* 277: 43771–43777

Perera EM, Martin H, Seeherunvong T, Kos L, Hughes IA, Hawkins JR, Berkovitz GD (2001) Tescalcin, a novel gene encoding a putative EF-hand Ca(2+)-binding protein, Col9a3, and renin are expressed in the mouse testis during the early stages of gonadal differentiation. *Endocrinology* 142: 455–463

Pouyssegur J, Sardet C, Franchi A, L'Allemain G, Paris S (1984) A specific mutation abolishing Na+/H+ antiport activity in hamster fibroblasts precludes growth at neutral and acidic pH. *Proc Natl Acad Sci USA* 81: 4833–4837

Putney LK, Denker SP, Barber DL (2002) The changing face of the Na+/H+ exchanger, NHE1: structure, regulation, and cellular actions. *Annu Rev Pharmacol Toxicol* 42: 527–552

Terwilliger TC (2000) Maximum-likelihood density modification. *Acta Crystallogr D* 56 (Part 8): 965–972

Terwilliger TC, Berendzen J (1999) Automated MAD and MIR structure solution. *Acta Crystallogr D* 55 (Part 4): 849–861

Vijay-Kumar S, Kumar VD (1999) Crystal structure of recombinant bovine neurocalcin. *Nat Struct Biol* 6: 80–88

Wakabayashi S, Bertrand B, Ikeda T, Pouyssegur J, Shigekawa M (1994) Mutation of calmodulin-binding site renders the Na+/H+ exchanger (NHE1) highly H(+)-sensitive and Ca2+ regulation-defective. *J Biol Chem* 269: 13710–13715

Wakabayashi S, Fafournoux P, Sardet C, Pouyssegur J (1992) The Na+/H+ antiporter cytoplasmic domain mediates growth factor signals and controls 'H(+)-sensing'. *Proc Natl Acad Sci USA* 89: 2424–2428

Wakabayashi S, Hisamitsu T, Pang T, Shigekawa M (2003a) Kinetic dissection of two distinct proton binding sites in Na+/H+ exchangers by measurement of reverse mode reaction. *J Biol Chem* 278: 43580–43585

Wakabayashi S, Hisamitsu T, Pang T, Shigekawa M (2003b) Mutations of Arg440 and Gly455/Gly456 oppositely change pH sensing of Na+/H+ exchanger 1. *J Biol Chem* 278: 11828–11835

Wakabayashi S, Pang T, Su X, Shigekawa M (2000) A novel topology model of the human Na(+)/H(+) exchanger isoform 1. *J Biol Chem* 275: 7942–7949

Wakabayashi S, Shigekawa M, Pouyssegur J (1997) Molecular physiology of vertebrate Na+/H+ exchangers. *Physiol Rev* 77: 51–74

Zachos NC, Tse M, Donowitz M (2005) Molecular physiology of intestinal Na+/H+ exchange. *Annu Rev Physiol* 67: 411–443

Zhang M, Tanaka T, Ikura M (1995) Calcium-induced conformational transition revealed by the solution structure of apo calmodulin. *Nat Struct Biol* 2: 758–767

Zhou W, Qian Y, Kunjilwar K, Pfaffinger PJ, Choe S (2004) Structural insights into the functional interaction of KChIP1 with Shal-type K(+) channels. *Neuron* 41: 573–586

Japanese Journal of Applied Physics
Vol. 45, No. 10A, 2006, pp. 8005–8009

Enhanced Magnification Angiography Using 20-μm-Focus Tungsten Tube

Toshiyuki ENOMOTO, Eiichi SATO[1], Yoshinobu SUMIYAMA, Katsuo AIZAWA[2], Manabu WATANABE, Etsuro TANAKA[3], Hidezo MORI[4], Hiroki KAWAKAMI[5], Toshiaki KAWAI[5], Takashi INOUE[6], Akira OGAWA[6] and Shigehiro SATO[7]

The 3rd Department of Surgery, Toho University School of Medicine, 2-17-6 Ohashi, Meguro-ku, Tokyo 153-8515, Japan
[1]*Department of Physics, Iwate Medical University, 3-16-1 Honchodori, Morioka 020-0015, Japan*
[2]*Tokyo Medical University [emeritus professor], 6-1-1 Shinjuku, Shinjuku-ku, Tokyo 160-8402, Japan*
[3]*Department of Nutritional Science, Faculty of Applied Bio-science, Tokyo University of Agriculture, 1-1-1 Sakuragaoka, Setagaya-ku, Tokyo 156-8502, Japan*
[4]*Department of Cardiac Physiology, National Cardiovascular Center Research Institute, 5-7-1 Fujishirodai, Suita, Osaka 565-8565, Japan*
[5]*Electron Tube Division #2, Hamamatsu Photonics K.K., 314-5 Shimokanzo, Iwata, Shizuoka 438-0193, Japan*
[6]*Department of Neurosurgery, School of Medicine, Iwate Medical University, 19-1 Uchimaru, Morioka 020-8505, Japan*
[7]*Department of Microbiology, School of Medicine, Iwate Medical University, 19-1 Uchimaru, Morioka 020-8505, Japan*

(Received April 10, 2006; accepted June 25, 2006; published online October 6, 2006)

A microfocus X-ray tube is useful for performing magnification radiography, and its X-ray generator (L9631, Hamamatsu Photonics) consists of a personal computer for controlling the tube voltage and current, and a main unit with a high-voltage circuit and a fixed-anode X-ray tube. The maximum tube voltage, current, and electric power were 110 kV, 800 μA, and 50 W, respectively. The focal-spot size was proportional to the electric power of the tube, and the size was approximately 20 μm with a power of 20 W. Using a 3-mm-thick aluminum filter, the X-ray intensity was 7.75 μGy/s at 1.0 m from the source with a tube voltage of 60 kV and a current of 100 μA. Because the peak photon energy was approximately 38 keV using the filter with a tube voltage of 60 kV, the bremsstrahlung X-rays were absorbed effectively by iodine-based contrast media at an iodine K-edge of 33.2 keV. Enhanced angiography was performed by fourfold magnification imaging with a computed radiography system using iodine-based microspheres 15 μm in diameter. In the angiography of nonliving animals, we observed fine blood vessels of approximately 100 μm with high contrast. [DOI: 10.1143/JJAP.45.8005]

KEYWORDS: high-contrast angiography, magnification digital radiography, microfocus X-ray tube, energy-selective imaging

1. Introduction

To perform high-speed medical radiography, several various flash X-ray generators using cold-cathode tubes have been developed.[1–4] In particular, quasi-monochromatic flash X-ray generators[5–10] have been designed to perform preliminary experiments for producing clean K-series X-rays, and higher-harmonic hard X-rays have been observed in a weakly ionized linear plasma of copper and nickel. However, in monochromatic flash radiography, difficulties in increasing X-ray duration and in performing X-ray computed tomography (CT) have been encountered.

Synchrotrons are capable of producing high-dose-rate monochromatic parallel X-ray beams using silicon crystals, and the beams have been applied to phase-contrast radiography[11,12] and enhanced K-edge angiography.[13,14] In angiography, monochromatic X-rays with photon energies ranging from 33.3 to 35 keV have been employed because the rays are absorbed effectively by iodine-based contrast media with an iodine K-edge of 33.2 keV.

Without using synchrotrons, phase-contrast radiography[15] for edge enhancement can be performed using a microfocus X-ray tube, and the enhancement has been achieved in mammography[16] with a computed radiography (CR) system[17] using a 100-μm-focus tube. Subsequently, we developed a cerium X-ray generator[18,19] to perform enhanced K-edge angiography using cone beams, and succeeded in observing fine blood vessels and coronary arteries with high contrast using cerium Kα-rays of 34.6 keV.

Although the magnification radiography is used to improve the spatial resolution in angiography utilizing a digital imaging system, it is difficult to design a small focus cerium tube for angiography. Therefore, narrow-photon-energy bremsstrahlung X-rays[20–22] with a peak energy of approximately 35 keV from a tungsten tube are used to perform high-contrast angiography.

In this research, we employed a microfocus tungsten tube, and performed enhanced magnification angiography by controlling bremsstrahlung X-ray spectra using an aluminum filter.

2. Principle of Enhanced Magnification Angiography

Figure 1 shows the mass attenuation coefficients of iodine at the selected energies; the coefficient curve is discontinuous at the iodine K-absorption edge of 33.2 keV. The effective bremsstrahlung X-rays for K-edge angiography are shown above the K-edge. Using a 3.0-mm-thick aluminum filter for absorbing soft X-rays, the peak photon energy of the bremsstrahlung rays increases to approximately 38 keV. In angiography, iodine contrast media in blood vessels easily absorb the rays, and soft bremsstrahlung rays are absorbed effectively by objects (muscles). Therefore, blood vessels are observed with high contrast. Subsequently, spatial resolution is improved by fourfold magnification imaging using a microfocus X-ray tube in conjunction with a CR system (Regius 150, Konica Minolta) at a sampling pitch of 87.5 μm.

3. Experimental Methods

The microfocus X-ray generator (L9631, Hamamatsu Photonics) consists of a personal computer and a system unit. The unit includes all the hardware in the X-ray generator, such as, a high-voltage circuit and a fixed anode X-ray tube. Tube voltage, current, and exposure time can be controlled by the computer. The maximum tube voltage, current, and electric power were 110 kV, 800 μA, and 50 W,